Analytical modelling of water wave interaction with a bottom-mounted surface-piercing porous cylinder in front of a vertical wall

Peiwen Cong[a, b*], Wei Bai[c] and Bin Teng[a]

[a] State Key Laboratory of Coastal and Offshore Engineering, Dalian University of Technology, Dalian 116024, China

[b] Department of Civil and Environmental Engineering, National University of Singapore, 117576, Singapore

[c] School of Computing, Mathematics and Digital Technology, Manchester Metropolitan University, Chester Street, Manchester M1 5GD, UK

Abstract

The interaction of water wave with a bottom-mounted surface-piercing porous cylinder near a rigid vertical wall is investigated by an analytical model newly developed in the present work within the context of linear potential flow theory. The image principle is used to transfer the original problem in bounded water into the equivalent problem of wave interaction with two symmetrical porous cylinders in open seas in the presence of bi-directional incident waves. The velocity potential is analytically derived by means of the eigenfunction expansion along with the matching technique. Furthermore, a new alternative method for the evaluation of wave force is developed via the application of the Haskind-Hanaoka relation to a porous structure. In this method, an auxiliary radiation potential is introduced to replace the diffraction potential for the calculation of wave force. The auxiliary radiation potential used here is due to the oscillation of a porous cylinder in front of a wall. The image principle is used again to search the solution of the wave radiation problem in bounded water and the original radiation problem is then transferred to that due to two porous cylinders undergoing in-phase or out-of-phase motions in open seas. After the validation of the

developed model, detailed parametric study is carried out. The porosity of the cylinder, incident wave heading and spacing between the cylinder and the wall are systematically adjusted to investigate their effects on the wave force as well as the wave elevation. The extension of our model to the case of a cylinder array in front of a wall has also been performed, and the associated phenomenon has been explored.

Key words:

Analytical model; Porous structure; Eigenfunction expansion method; Image principle; Bounded water

1. Introduction

As porous structures are effective at dissipating the unwanted wave energy and minimizing the environmental impact, they have been widely constructed for the purpose of shore protection. Currently, porous structures have constituted an important class of maritime structures and a good understanding of the hydrodynamic properties of porous structures has long been demanded. Various research works have been performed to investigate the interaction of water wave with porous structures.

The use of a porous plate as a breakwater has been an attractive option. A porous horizontal plate submerged at a certain distance below the free surface could not only largely reduce the reflection coefficient and wave action but also make the transmission coefficient remain at a low level (Yu and Chwang, 1994). In addition, it allows water exchange above and below it, thus retains water quality and prevents seawater pollution (Cho and Kim, 2013). Besides the horizontal porous plate, a vertical plate with suitable porosity has also been gradually used as a breakwater. The application of a vertical porous plate can weaken the unexpected surface fluctuation inside the harbor, which is important for the safe maneuvering of vessels (Li et al., 2006). So far, many researchers have assessed the functional performance of a horizontal or vertical porous plate as a breakwater, such as Neves et al. (2000), Cho and Kim (2008), Kee (2009), Evans (2011), Liu et al. (2011) and Zhao et al. (2017).

At the same time, the use of a perforated caisson as a breakwater has also been a very attractive option. Compared with impermeable structures, structures with perforated parts are normally considered to be easier to construct and more economical. In addition, the use of perforated structures can avoid local scour as well as the increase in wave agitation due to the considerable wave reflection (Sankarbabu et al., 2008). Jarlan-type breakwater consisting of a perforated front wall and an impermeable rear wall (Jarlan, 1961) has been the earliest perforated caisson breakwater. Since then much effort has been made by researchers in quantifying the functional performance of the perforated caisson type breakwater and other innovative configurations have been reported, such as the concentric porous cylinder system (Wang and Ren, 1994; Song and Tao, 2007; Ning et al., 2017; Liu et al., 2018), perforated caisson with inner plates (Yip and Chang, 2000; Liu et al., 2007b) and arrays of porous columns with rectangular or cylindrical sections (Williams and Li, 2000; Teng et al., 2004b; Liu et al. 2007a; Sankarbabu et al., 2008; Chen et al., 2011).

As mentioned above, a porous cylinder or cylinder array can be a promising solution of a breakwater. Many studies on the behavior of a porous cylinder or cylinder array in waves have been conducted. Wang and Ren (1994) analytically investigated the wave interaction with a two-cylinder system consisting of an exterior porous cylinder with thin thickness and an inner concentric impermeable cylinder. Darwiche et al. (1994) also conducted research work related to a concentric porous cylinder system, in which the exterior cylinder is porous near the free surface but becomes impermeable in the lower part. Williams and Li (1998) extended the analysis in Darwiche et al. (1994) to the case in which the inner cylinder is mounted on a storage tank. Williams and Li (2000) dealt with the problem of the wave interaction with multiple porous cylinders based on the eigenfunction expansion method proposed by Linton and Evans (1990). Zhong and Wang (2006) developed a theoretical model to study the interaction of solitary waves with a concentric porous cylinder system. Chen et al. (2011) used the null-field integral formulation to study the near trapping phenomenon by an array of porous cylinders and assessed the porous effects and the disorder of the layout on the near trapping phenomenon. Mandal et al. (2013) applied the Fourier-Bessel series expansion method in conjunction with the least square approximation to investigate the wave interaction with an exterior porous and flexible thin cylinder protecting an inner impermeable cylinder. Liu et al. (2018) presented an analytical method for deriving the velocity potential for waves traveling through a concentric porous cylinder system with arbitrary smooth section.

The hydrodynamics of porous structures in open seas have been widely studied. In the meantime, porous structures, situated at a finite distance from a rigid wall, have also been gradually built in various projects, such as ship navigation or as an artificial breeding or nursing ground for sea animals (Koley, et al., 2015). However, the study on porous structures in front of a rigid wall is very rare, and the problem is still not well understood. The vertical cylinder is widely used in the maritime engineering. Especially, the porous cylinder can be adopted as a breakwater in the harbour area to ensure the natural water circulation for the mitigation of environmental pollutions. Therefore, an analytical solution is developed in this study to explore the phenomenon of water wave interaction with a bottom-mounted surface-piercing porous cylinder near a rigid vertical wall. The wall is assumed to be fully reflective infinite vertical and can be used to approximate a wharf (Teng et al., 2004a; Zheng and Zhang, 2015). In this new method, the image principle is used to transfer the original problem in bounded water into the equivalent problem of wave interaction with two porous cylinders in open seas in the presence of bi-directional incident waves. The eigenfunction expansion method along with the matching technique is used to derive the velocity potential. In the equivalent problem in open seas, the relationship between the Fourier coefficients related to the real and image cylinders has been established, based on which it can demonstrate that the no-flow condition is satisfied on the vertical wall. Furthermore, a new alternative method is developed to evaluate the wave force using the Haskind-Hanaoka relation. The Haskind-Hanaoka relation was originally established for impermeable bodies (Mei, 2005), and extended to the case of a porous structure by Zhao et al. (2011). In this method, the wave fore is evaluated based on the introduction of an auxiliary radiation potential and the explicit solution of the diffraction potential is not required. The image principle is used again to solve the wave radiation problem due to the oscillation of a porous cylinder in front of a wall. In the equivalent radiation problem in open seas, the no-flow condition on the vertical wall has also been discussed. By comparing the wave force obtained by these two approaches, the validity of the present model is examined. With the developed model, numerical analysis concerning a porous cylinder in front of a wall is performed in detail to investigate the effects of porosity, incident wave heading and distance between the cylinder and the wall on the hydrodynamic properties of the porous cylinder. The extension of our model to the case of a cylinder array has also been performed in this study. Numerical results related to an array of porous cylinders in front of a wall are also presented.

Following the introduction, the mathematical description of the problem is presented in Section 2. The analytical solution of the velocity potential is introduced in Section 3, which is followed by the calculation of wave force and wave elevation based on the obtained velocity potential. The alternative method for the calculation of wave force is discussed in detail in Section 5. Section 6 shows convergence test and validation of the analytical model, while the parametric study is carried out thereafter in Section 7, with conclusions drawn in Section 8.

2. Mathematical model

Consider a bottom-mounted, surface-piercing, thin-walled porous cylinder of radius a situated near a vertical wall (see Fig. 1). The incident wave of amplitude A and angular frequency ω propagates in the water of constant depth d. The minimum distance between the cylinder and the wall is e. As the vertical wall is assumed to be infinite long and fully reflective, the hydrodynamic problem can then be transformed into an equivalent problem of two symmetrical cylinders in the unbounded fluid domain (Teng et al., 2004a), as shown in Fig. 2 where the left cylinder is the real cylinder, while the right cylinder is the image cylinder. A global Cartesian coordinate system ($Oxyz$) is adopted with an origin located at the middle of the two cylinders on the still free surface.

The z-axis directs vertically upwards. The centers of the real and image cylinders are located at ($-R$, 0, 0) and (R, 0, 0), respectively, on the still free surface. Two polar coordinates $O_jr_j\theta_jz_j$ (j = 1, 2) are defined with their origins locating at ($-R$, 0, 0) and (R, 0, 0) respectively in the global coordinate system. The z_j-axis is defined positive upwards. In this system, the two symmetrical cylinders are subjected to two incident wave trains of amplitude A and angular frequency ω propagating in the direction β and $\pi - \beta$, respectively, relative to the positive Ox axis.

It is assumed that the fluid is inviscid and incompressible with a constant density ρ, and that the fluid motion is irrotational. Then, the fluid velocity can be described by the gradient of the velocity potential Φ satisfying Laplace's equation

$$\nabla^2\Phi(\mathbf{x},\ t) = 0. \tag{1}$$

By considering linear harmonic incident wave, the time factor can be separated out and the velocity potential is then expressed as

$$\Phi(\mathbf{x},\ t) = \mathrm{Re}\left[\phi(r,\ \theta,\ z)e^{-i\omega t}\right], \tag{2}$$

where Re[] denotes the real part of a complex expression; ω represents the wave angular frequency; $i = \sqrt{-1}$.

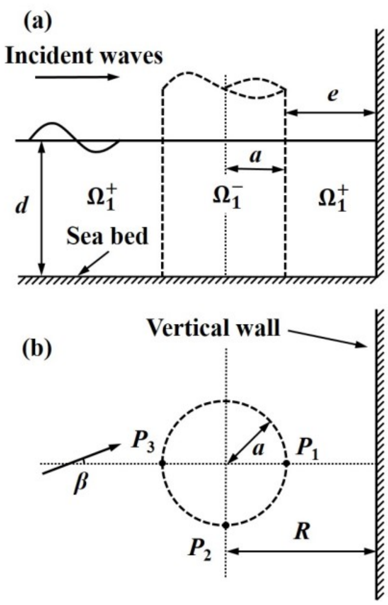

Fig. 1 Definition sketch for a porous cylinder near a vertical wall: (a) side view and (b) plane view

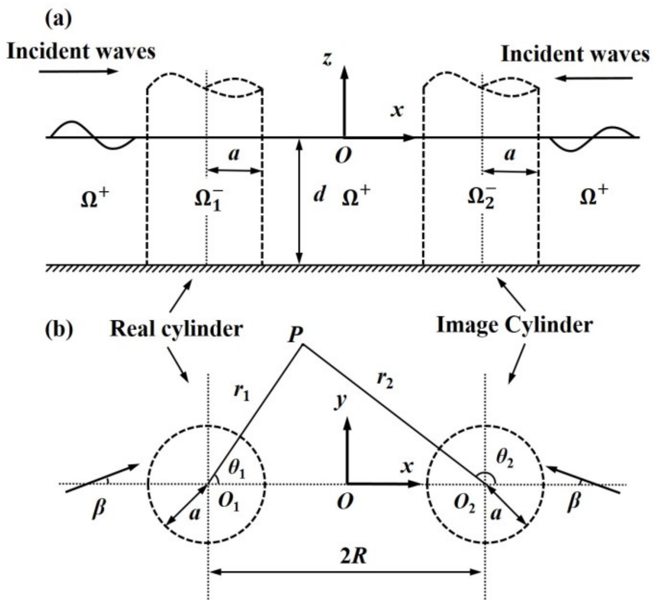

Fig. 2 Definition sketch for two symmetrical cylinders in open seas: (a) side view and (b) plane view

As shown in Fig. 2(a), the unbounded fluid domain is divided into 3 sub-domains: one single exterior region, Ω^+, and two interior regions, Ω_1^- and Ω_2^-. The interior regions are those inside the real and image cylinders respectively and defined by $0 \le r_j \le a_j$, j = 1, 2. a_1 and a_2 are the radii of the real and image cylinders, respectively, and in this study $a_1 = a_2 = a$. The velocity potential in the exterior region is denoted by ϕ^+, while that in the interior region is denoted by ϕ_j^- (j =1, 2). Besides Laplace's equation, the velocity potential is also required to satisfy appropriate boundary conditions on the free surface and the impermeable sea bed, namely

$$\frac{\partial \phi^+}{\partial z} = \frac{\omega^2}{g}\phi^+, \quad \frac{\partial \phi_j^-}{\partial z} = \frac{\omega^2}{g}\phi_j^-, \quad \text{on } z = 0, \quad j = 1,\ 2; \tag{3}$$

$$\frac{\partial \phi^+}{\partial z} = 0, \quad \frac{\partial \phi_j^-}{\partial z} = 0, \quad \text{on } z = -d, \quad j = 1,\ 2, \tag{4}$$

where g is the acceleration due to gravity.

To model the flow separation through porous materials, a quadratic law, relating the pressure drops to the traversing velocity, has been proposed in some studies, such as Molin (2011), An and Faltinsen (2013). The numerical predictions of hydrodynamic coefficients, added mass and damping, based on the application of quadratic pressure drops are in good agreement with the experimental results for porous stabilizer, plate or disk undergoing forced motions (Molin and Legras, 1990; Molin et al., 2007; An and Faltinsen, 2013; Molin and Remy, 2013). On the other hand, a linear relation between the pressure drop and the cross-flow velocity has also been developed by researchers, such as Chwang (1983) by making use of the Darcy's law and Yu (1995) by applying the convection-neglected and porous-effect-modelled Euler equation. The linear law has been applied in many studies to model the wave interaction with structures consisting of porous cylinders, and the numerical predictions of wave force and wave runup agree well with the experimental measurements (Sankarbabu, 2007; Vijayalakshmi et al., 2007; Zhao et al., 2010; Zhao et al., 2012). A bottom-mounted porous cylinder located in bounded water is concerned in this study, the assumption that the normal fluid velocity passing through a thin porous wall is linearly proportional to the pressure difference across the thickness of the wall is therefore adopted. Then, according to Chwang (1983) and Yu (1995), the boundary condition on the porous wall can be expressed as follows

$$\frac{\partial \phi^+}{\partial r} = \frac{\partial \phi_j^-}{\partial r} = i\kappa_0 G_0 \left(\phi_j^- - \phi^+ \right), \quad \text{on } r{=}a_j, \quad j = 1,\ 2, \tag{5}$$

where κ_0 is the wave number satisfying the dispersion relation $\omega^2 = g\kappa_0 \tanh \kappa_0 d$; G_0 is the complex linearized porous effect parameter. The real and imagery parts of G_0 represent the resistance and inertial effects of the porous wall and are relevant to the energy dissipation and phase change respectively (Li et al., 2006). The experimental studies of Li et al. (2002, 2006) suggested that the real part of G_0 dominates the imaginary part. Therefore, it is assumed that the imaginary part of G_0 is zero in this study. It is obvious that, when $|G_0|$ approaches 0, the cylinder wall tends to be solid; while, when $|G_0|$ approaches infinity, the cylinder becomes entirely transparent. It is also noted that the continuity of the normal fluid velocity between interior and exterior subdomains is mathematically fulfilled by Eq. (5).

3. Analytical solution of velocity potential

The presence of the stationary body in the fluid results in diffraction of the incident wave. The velocity potential in the exterior region, ϕ^+, can then be decomposed into the incident and diffraction potentials respectively, i.e.,

$$\phi^+ = \phi_I + \phi_D, \tag{6}$$

in which, ϕ_I represents the incident potential; ϕ_D represents the diffraction potential in the exterior region. In addition to the boundary conditions in Eqs. (3), (4) and (5), the diffraction potential is also required to satisfy the Sommerfeld radiation condition at a large radial distance from the structure

$$\lim_{r\to\infty}\sqrt{r}\left(\frac{\partial \phi_D}{\partial r} - i\kappa_0\phi_D\right) = 0. \tag{7}$$

Considering two undisturbed incident waves propagating with the directions β and $\pi-\beta$, respectively, in the constant water depth d, ϕ_I can be written as:

$$\phi_I = -\frac{iAg}{\omega} Z_0(\kappa_0 z) e^{i\kappa_0 y\sin\beta}\left(e^{i\kappa_0 x\cos\beta} + e^{-i\kappa_0 x\cos\beta}\right), \tag{8}$$

in which, $Z_0(\kappa_0 z)$ is an orthonormal function given at the interval $[-d, 0]$ and defined by

$$Z_0(\kappa_0 z) = \frac{\cosh\kappa_0(z+d)}{\cosh\kappa_0 d}. \tag{9}$$

In the jth local polar coordinate system, ϕ_I can be rewritten as

$$\phi_I(r_j, \theta_j, z_j) = \sum_{m=-\infty}^{+\infty} \Lambda_m^j J_m(\kappa_0 r_j) Z_0(\kappa_0 z_j) e^{im\theta_j}, \tag{10}$$

in which

$$\Lambda_m^j = -\frac{iAg}{\omega}\left[I_j^\beta e^{-im\beta} + I_j^{\pi-\beta} e^{-im(\pi-\beta)}\right] i^m. \tag{11}$$

In Eq. (11), I_j^β and $I_j^{\pi-\beta}$ are the phase correction factors associated with the jth cylinder and defined by

$$I_j^\beta = e^{i\kappa_0(x_j\cos\beta + y_j\sin\beta)};\quad I_j^{\pi-\beta} = e^{i\kappa_0(-x_j\cos\beta + y_j\sin\beta)}, \tag{12}$$

in which, $(x_j, y_j, 0)$ is the center of the jth cylinder on the free surface in the global coordinate system. Following Linton and Evans (1990), the diffraction potential, ϕ_D, is expressed as a summation of waves emanating from different cylinders

$$\phi_D = \sum_{j=1}^{N=2} \sum_{m=-\infty}^{+\infty} A_m^j C_m^j H_m\left(\kappa_0 r_j\right) Z_0\left(\kappa_0 z_j\right) e^{im\theta_j}. \tag{13}$$

In Eq. (13), N represents the total number of cylinders in the imaginary system and it is two times the number of cylinders in the original problem in bounded water, N_b. Considering the situation shown in Figs. 1 and 2, N_b and N are equal to 1 and 2 respectively; A_m^j are the unknown coefficients; the factor C_m^j is introduced to simplify the expression of wave force that will be obtained later and defined by

$$C_m^j = \frac{J_m'\left(\kappa_0 a_j\right)}{H_m'\left(\kappa_0 a_j\right)}, \tag{14}$$

where, $H_m(x)$ stands for the first kind of Hankel functions of order m.

In Eq. (13), the waves emanating from the two cylinders are expressed in their respective local polar coordinate systems. To facilitate the application of the body-surface boundary condition, it is necessary to express all terms in Eq. (13) in the same local coordinate system. This can be accomplished by using Graf's addition theorem for Bessel functions (Abramowitz and Stegun, 1972)

$$H_n\left(\kappa_0 r_k\right) e^{in\theta_k} = \sum_{m=-\infty}^{+\infty} H_{m+n}\left(\kappa_0 R_{kj}\right) J_m\left(\kappa_0 r_j\right) e^{i\left(n\alpha_{kj} + m\alpha_{jk}\right)} e^{-im\theta_j}. \tag{15}$$

In Eq. (15), R_{kj}, equal to $2R$, represents the distance between the centers of the two cylinders; α_{jk} is the angle between the x-axis and the vector from the center of cylinder j to that of cylinder k. Eq. (15) is valid for $r_j < R_{kj}$ and this is obviously true on the wall surface of the cylinders. The velocity potential in the exterior region, ϕ^+, can then be expressed in the jth local polar coordinate system as

$$\phi^+\left(r_j, \theta_j, z_j\right) = \sum_{m=-\infty}^{+\infty} \left[\Lambda_m^j J_m\left(\kappa_0 r_j\right) + A_m^j C_m^j H_m\left(\kappa_0 r_j\right) + \sum_{\substack{k=1 \\ k \neq j}}^{N=2} \sum_{n=-\infty}^{+\infty} A_n^k C_n^k \Delta_{m,n}^{j,k} J_m\left(\kappa_0 r_j\right) \right] Z_0\left(\kappa_0 z_j\right) e^{im\theta_j}, \tag{16}$$

in which,

$$\Delta_{m,n}^{j,k} = H_{n-m}\left(\kappa_0 R_{kj}\right)\left(-1\right)^m e^{i\left(n\alpha_{kj} - m\alpha_{jk}\right)}. \tag{17}$$

According to Williams and Li (2000), the velocity potential in the jth interior region,

ϕ_j^- can be expressed as

$$\phi_j^-\left(r_j,\ \theta_j,\ z_j\right)=\sum_{m=-\infty}^{+\infty} B_m^j J_m\left(\kappa_0 r_j\right) Z_0\left(\kappa_0 z_j\right) e^{im\theta_j}, \tag{18}$$

in which, B_m^j are the unknown coefficients. The remaining task is to determine the unknown coefficients in Eqs. (16) and (18). By applying Eq. (5) and utilizing the orthogonal properties of sin$m\theta$, cos$m\theta$ and the vertical eigenfunctions, the following relationships between A_m^j and B_m^j can be yielded for j = 1, 2

$$\Lambda_m^j + A_m^j + \sum_{\substack{k=1\\k\neq j}}^{N=2} \sum_{n=-\infty}^{+\infty} A_n^k C_n^k \Delta_{m,\,n}^{j,\,k} = B_m^j; \tag{19a}$$

$$B_m^j\left[iG_0-\frac{J_m'\left(\kappa_0 a_j\right)}{J_m\left(\kappa_0 a_j\right)}\right]=iG_0\left[\Lambda_m^j + A_m^j C_m^j \frac{H_m\left(\kappa_0 a_j\right)}{J_m\left(\kappa_0 a_j\right)}+\sum_{k=1,\,k\neq j}^{N=2} \sum_{n=-\infty}^{+\infty} A_n^k C_n^k \Delta_{m,\,n}^{j,\,k}\right]. \tag{19b}$$

By combining above equations and making use of the Wronskian relations for Bessel functions, an infinite system of equations can be obtained. In order to find a solution to the unknown coefficients A_m^j and B_m^j, the system has to be truncated and only $2M$ + 1 Fourier modes are considered for j = 1, 2 in the present study, i.e.

$$A_m^j\left[1+\frac{2G_0}{\pi\kappa_0 a_j}\frac{1}{J_m'\left(\kappa_0 a_j\right)H_m'\left(\kappa_0 a_j\right)}\right]+\sum_{\substack{k=1\\k\neq j}}^{N=2} \sum_{n=-M}^{+M} A_n^k C_n^k \Delta_{m,\,n}^{j,\,k} = -\Lambda_m^j; \tag{20a}$$

$$B_m^j = -\frac{2G_0}{\pi\kappa_0 a_j}\frac{A_m^j}{J_m'\left(\kappa_0 a_j\right)H_m'\left(\kappa_0 a_j\right)}. \tag{20b}$$

Therefore, two sets of linear equations of equivalent numbers of unknowns can be established. The linear algebraic equation system can then be solved by means of the standard matrix techniques. With the obtained coefficients, the velocity potential in each region can be determined. The no-flow condition on the vertical wall in the equivalent problem in open seas is discussed in the Appendix. In the imaginary system in open seas, due to the symmetry of the system, relationships between the Fourier coefficients related to the real and image cylinders, A_m^1 and A_m^2, have been established in the Appendix (see Eq. (A6)). Based on the relationships between A_m^1 and A_m^2, the no-flow condition on the vertical wall can be demonstrated.

4. Calculation of wave force and wave elevation

Once the solution of velocity potential is obtained, some other physical quantities of interest (e.g., wave elevation, pressure distribution, etc.) may immediately be found. The wave force and moment can be obtained by the integral of pressure difference between two sides of the body surface. Then, the amplitudes of the horizontal wave forces on the real cylinder, f_x and f_y, are given by

$$\begin{Bmatrix} f_x \\ f_y \end{Bmatrix} = -i\omega\rho a_1 \int_{-d}^{0}\int_{0}^{2\pi} \left(\phi^+ - \phi_1^-\right)\Big|_{r_1=a_1} \begin{Bmatrix} \cos\theta_1 \\ \sin\theta_1 \end{Bmatrix} dz_1 d\theta_1. \tag{21}$$

Meanwhile, the amplitudes of the wave moments on the real cylinder, m_x and m_y, can be determined according to

$$\begin{Bmatrix} m_x \\ m_y \end{Bmatrix} = i\omega\rho a_1 \int_{-d}^{0}\int_{0}^{2\pi} \left(\phi^+ - \phi_1^-\right)\Big|_{r_1=a_1} \begin{Bmatrix} \sin\theta_1 \\ -\cos\theta_1 \end{Bmatrix} z_1 dz_1 d\theta_1. \tag{22}$$

For the calculation of m_x and m_y, the rotation center is located at the center of the real cylinder on the still free surface.

Following Linton and Evans (1990) and Williams and Li (2000), the expression of the velocity potential on the outer wall surface of the real cylinder is simplified by taking Eq. (20a) into Eq. (16) and making use of the Wronskian relationships for the Bessel functions, which is given by

$$\phi^+\left(a_1, \theta_1, z_1\right) = -\sum_{m=-\infty}^{+\infty} \frac{2A_m^1}{\pi\kappa_0 a_1 H_m'\left(\kappa_0 a_1\right)} \left[\frac{J_n\left(\kappa_0 a_1\right)}{J_n'\left(\kappa_0 a_1\right)} G_0 + i\right] Z_0\left(\kappa_0 z_1\right) e^{im\theta_1}. \tag{23}$$

Then, evaluation of the integral in Eq. (21) gives:

$$\begin{Bmatrix} f_x \\ f_y \end{Bmatrix} = \begin{Bmatrix} 1 \\ -i \end{Bmatrix} \frac{2\omega\rho}{H_1'\left(\kappa_0 a_1\right)} \frac{\tanh\kappa_0 d}{\kappa_0^2} \left(A_{-1}^1 \begin{Bmatrix} - \\ + \end{Bmatrix} A_1^1\right). \tag{24}$$

Similarly, Eq. (22) can be rewritten as:

$$\begin{Bmatrix} m_x \\ m_y \end{Bmatrix} = \begin{Bmatrix} i \\ 1 \end{Bmatrix} \frac{2\omega\rho}{H_1'\left(\kappa_0 a_1\right)} \frac{1-\cosh\kappa_0 d}{\kappa_0^3 \cosh\kappa_0 d} \left(A_{-1}^1 \begin{Bmatrix} + \\ - \end{Bmatrix} A_1^1\right). \tag{25}$$

The wave elevation, η, can be given in terms of the velocity potential. Around the real cylinder, η can be efficiently evaluated based on the following expressions

$$\eta = Ae^{i\kappa_0 y\sin\beta}\left(e^{i\kappa_0 x\cos\beta}+e^{-i\kappa_0 x\cos\beta}\right)+\frac{i\omega}{g}\sum_{j=1}^{N=2}\sum_{m=-\infty}^{+\infty} A_m^j C_m^j H_m\left(\kappa_0 r_j\right)e^{im\theta_j}, \quad \text{in } \Omega^+; \quad (26a)$$

$$\eta = \frac{i\omega}{g}\sum_{m=-\infty}^{+\infty} B_m^1 J_m\left(\kappa_0 r_1\right)e^{im\theta_1}, \quad \text{in } \Omega_1^-. \quad (26b)$$

In Eq. (26a), the first part on the right-hand side results from the incident wave travelling to the vertical wall without the cylinder, while the remaining parts are due to the wave emanating from the real and image cylinders respectively.

5. Alternative method for the calculation of wave force

According to Eqs. (24) and (25), it is noted that the wave moment can be expressed in terms of wave force. Therefore, discussion is only made on the wave force in this work. A new alternative method for the calculation of wave force is developed in this section. The method is based on the application of Green's second identity with the use of an auxiliary radiation potential and does not require the explicit solution of diffraction potential. For the evaluation of the auxiliary radiation potential, the porous cylinder in front of the wall is no longer fixed and allowed to move in specific directions. The radiation potential due to the harmonic oscillation in the *x*- and *y*-directions (surge and sway motions) are needed in the calculation of f_x and f_y, respectively.

Based on the image principle, the wave radiation problem discussed here can be transformed to the equivalent one due to the motions of two symmetrical cylinders in unbounded fluid domain. The two cylinders undergo out-of-phase surge motions or in-phase sway motions. Hereinafter, ψ^+ represents the auxiliary radiation potential in the exterior region. Meanwhile, ψ_j^- represents that inside the real (j = 1) and image (j = 2) cylinders. The auxiliary radiation potential is governed by the Laplace’s equation and satisfies the homogeneous boundary conditions on the free surface and seabed as in Eqs. (3) and (4). In addition, they also have to satisfy the Somerfield condition at the far field. On the porous wall surface of the cylinder, the following conditions have to be satisfied (see, Zhao et al., 2011)

$$\frac{\partial \psi^{+}}{\partial r}=\frac{\partial \psi_j^{-}}{\partial r}=u_j\left(\theta_j\right)+i\kappa_0 G_0\left(\psi_j^{-}-\psi^{+}\right), \quad \text{on } r_j=a_j. \tag{27}$$

When the cylinders undergo out-of-phase surge motions, $u_j\left(\theta_j\right)$ is defined by

$$u_j\left(\theta_j\right)=\begin{cases}\cos\theta_j, & j=1;\\ -\cos\theta_j, & j=2.\end{cases} \tag{28}$$

When undergoing in-phase sway motions, $u_j\left(\theta_j\right)$ is given by

$$u_j\left(\theta_j\right)=\sin\theta_j, \quad j=1,\ 2. \tag{29}$$

Following Teng et al. (2004a), the approach of separation of variables is applied in each region and yields the velocity potential expressed by the orthogonal series

$$\psi^{+}=\sum_{j=1}^{N=2}\left\{\sum_{m=-\infty}^{+\infty}\left[\hat{A}_{m,\,0}^{j}H_m\left(\kappa_0 r_j\right)Z_0\left(\kappa_0 z_j\right)+\sum_{l=1}^{\infty}\hat{A}_{m,\,l}^{j}K_m\left(\kappa_l r_j\right)Z_l\left(\kappa_l z_j\right)\right]e^{im\theta_j}\right\}; \tag{30a}$$

$$\psi_j^{-}=\sum_{m=-\infty}^{+\infty}\left[\hat{B}_{m,\,0}^{j}J_m\left(\kappa_0 r_j\right)Z_0\left(\kappa_0 z_j\right)+\sum_{l=1}^{\infty}\hat{B}_{m,\,l}^{j}I_m\left(\kappa_l r_j\right)Z_l\left(\kappa_l z_j\right)\right]e^{im\theta_j}, \quad j=1,\ 2, \tag{30b}$$

in which, $\hat{A}_{m,\,l}^{j}$ and $\hat{B}_{m,\,l}^{j}$ $(l\geq 0)$ are the unknown coefficients; $K_m\left(x\right)$ and $I_m\left(x\right)$ stand for the first and second kind of modified Hankel functions of order m respectively; κ_l $(l\geq 1)$ are the positive real roots of $\omega^2=-g\kappa_l\tan\kappa_l d$; $Z_l\left(\kappa_l z_j\right)$ for $l\geq 1$ are defined by

$$Z_l\left(\kappa_l z_j\right)=\frac{\cos\kappa_l\left(z_j+d\right)}{\cos\kappa_l d}. \tag{31}$$

Those expressions in Eq. (30) are developed to satisfy the Laplace's equation and all the boundary conditions except that satisfied on the porous wall surface of the cylinder. The application of the Graf's addition theorem for Bessel functions yields

$$K_n\left(\kappa_l r_k\right)e^{in\theta_k}=\sum_{m=-\infty}^{+\infty}K_{m+n}\left(\kappa_l R_{kj}\right)I_m\left(\kappa_l r_j\right)e^{i\left(n\alpha_{kj}+m\alpha_{jk}\right)}e^{-im\theta_j}. \tag{32}$$

Eq. (32) is valid in the vicinity of the jth cylinder, ie, $r_j<R_{kj}$. By substituting Eqs. (15) and (32) into Eq. (30a) and replacing m by $-m$, ψ^{+} can be expressed in the jth coordinate system as follows

$$\psi^{+}\left(r_j,\ \theta_j,\ z_j\right)=\sum_{m=-\infty}^{+\infty}\left[\hat{A}_{m,\,0}^{j}H_m\left(\kappa_0 r_j\right)+\sum_{\substack{k=1\\k\neq j}}^{N=2}\sum_{n=-\infty}^{+\infty}\hat{A}_{n,\,0}^{k}\Delta_{m,\,n}^{j,\,k}J_m\left(\kappa_0 r_j\right)\right]Z_0\left(\kappa_0 z_j\right)e^{im\theta_j}$$
$$+\sum_{m=-\infty}^{+\infty}\sum_{l=1}^{\infty}\left[\hat{A}_{m,\,l}^{j}K_m\left(\kappa_l r_j\right)+\sum_{\substack{k=1\\k\neq j}}^{2}\sum_{n=-\infty}^{+\infty}\hat{A}_{n,\,l}^{k}\Delta_{m,\,n,\,l}^{j,\,k}I_m\left(\kappa_l r_j\right)\right]Z_l\left(\kappa_l z_j\right)e^{im\theta_j}, \tag{33}$$

in which

$$\Delta_{m,\,n,\,l}^{j,\,k}=K_{n-m}\left(\kappa_l R_{kj}\right)e^{i\left(n\alpha_{kj}-m\alpha_{jk}\right)},\quad l\geq 1. \tag{34}$$

The unknown coefficients in Eq. (33) can be determined by imposing the boundary condition satisfied on the body surface. By utilizing the orthogonal property of sin$m\theta$, cos$m\theta$ and the vertical eigenfunctions, the following relationships between $\hat{A}_m^j$ and $\hat{B}_m^j$ can be yielded

$$\hat{A}_{m,\,0}^{j}\left[H_m'\left(\kappa_0 a_j\right)+\frac{2G_0}{\pi\kappa_0 a_j J_m'\left(\kappa_0 a_j\right)}\right]+\sum_{\substack{k=1\\k\neq j}}^{N=2}\sum_{n=-M}^{+M}\hat{A}_{n,\,0}^{k}\Delta_{m,\,n}^{j,\,k}J_m'\left(\kappa_0 a_j\right)=s_{m,\,0}^{j}; \tag{35a}$$

$$-\frac{2G_0}{\pi\kappa_0 a_j J_m'\left(\kappa_0 a_j\right)J_m'\left(\kappa_0 a_j\right)}\hat{A}_{m,\,0}^{j}+\frac{s_{m,\,0}^{j}}{J_m'\left(\kappa_0 a_j\right)}=\hat{B}_{m,\,0}^{j}, \tag{35b}$$

and

$$\hat{A}_{m,\,l}^{j}\left[K_m'\left(\kappa_l a_j\right)+\frac{i\kappa_0 G_0}{\left(\kappa_l\right)^2 a_j I_m'\left(\kappa_l a_j\right)}\right]+\sum_{\substack{k=1\\k\neq j}}^{N=2}\sum_{n=-M}^{+M}\hat{A}_{n,\,l}^{k}\Delta_{m,\,n,\,l}^{j,\,k}I_m'\left(\kappa_l a_j\right)=s_{m,\,l}^{j}, \tag{36a}$$

$$-\frac{i\kappa_0 G_0}{\left(\kappa_l\right)^2 a_j I_m'\left(\kappa_l a_j\right)I_m'\left(\kappa_l a_j\right)}\hat{A}_{m,\,l}^{j}+\frac{s_{m,\,l}^{j}}{I_m'\left(\kappa_l a_j\right)}=\hat{B}_{m,\,l}^{j}. \tag{36b}$$

When the cylinders undergo out-of-phase surge motions, $s_{m,\,l}^{j}$ is given by

$$s_{m,\,l}^{j}=\begin{cases}\Gamma_l, & m=\pm 1, \quad j=1;\\ -\Gamma_l, & m=\pm 1, \quad j=2;\\ 0, & m\neq\pm 1, \quad j=1,\ 2,\end{cases} \tag{37}$$

in which

$$\Gamma_l=\begin{cases}\dfrac{\sinh 2\kappa_0 d}{\kappa_0\left(2\kappa_0 d+\sinh 2\kappa_0 d\right)}, & l=0;\\[2ex] \dfrac{\sin 2\kappa_l d}{\kappa_l\left(2\kappa_l d+\sin 2\kappa_l d\right)}, & l\geq 1.\end{cases} \tag{38}$$

When undergoing in-phase sway motions, $s_{m,l}^{j}$ is given by

$$s_{m,l}^{j}=\begin{cases}-i\Gamma_{l}, & m=1, \quad j=1,\ 2;\\ i\Gamma_{l}, & m=-1, \quad j=1,\ 2;\\ 0, & m\neq\pm 1, \quad j=1,\ 2.\end{cases} \tag{39}$$

The unknown coefficients can thereby be solved from these complex equations. With those coefficients being available, the radiation potential at any position in the fluid domain can be determined. For the wave radiation problem due to the motions of two symmetrical cylinders in open seas, relationships between the Fourier coefficients related to the real and image cylinders, $A_{m,l}^{1}$ and $A_{m,l}^{2}$, have been established in the Appendix (see Eqs. (A12) and (A15)). Discussion on the no-flow condition at the vertical wall in the equivalent radiation problem in open seas has also been made in the Appendix.

We next return to the problem of wave diffraction by a porous cylinder situated near a vertical wall, as depicted in Fig. 1. As shown in Fig. 1(a), the bounded fluid domain is further divided into the subdomains inside and outside the real cylinder, which are denoted by Ω_1^- and Ω_1^+ respectively. In Ω_1^+, the application of the Green's second identify to the diffraction potential, ϕ_D^+, and the auxiliary radiation potential, ψ^+, leads to

$$\iint_{S_{1,b}^{+}\cup S_{1,d}^{+}\cup S_{1,f}^{+}\cup S_{w}\cup S_{1,\infty}^{+}}\left(\phi_D^{+}\frac{\partial\psi^{+}}{\partial n}-\psi^{+}\frac{\partial\phi_D^{+}}{\partial n}\right)ds=0. \tag{40}$$

In Eq. (40), $S_{1,b}^{+}$ is the outer wall surface of the real cylinder; $S_{1,d}^{+}$ and $S_{1,f}^{+}$ represent the seabed and free surface in Ω_1^+; S_w represents the infinite vertical wall; $S_{1,\infty}^{+}$ is a semi cylindrical surface at far field and defined by $-d\le z\le 0$, $\pi/2\le\theta<3\pi/2$ and $r\to+\infty$; **n** is the unit vector normal to the surface pointing out of the fluid domain. As ϕ_D^+ and ψ^+ both satisfy the Sommerfeld condition at far field, the integral over $S_{1,\infty}^{+}$ oscillates towards zero as the radius of $S_{1,\infty}^{+}$ goes to infinity. In addition, as the infinite vertical wall is fully reflective, it is obviously that the integral over S_w is zero. Then imposing the seabed and free surface boundary conditions on ϕ_D^+ and ψ^+ gives

$$\iint_{S_{1,b}^{+}} \left(\phi_D^{+} \frac{\partial \psi^{+}}{\partial r} - \psi^{+} \frac{\partial \phi_D^{+}}{\partial r} \right) ds = 0. \tag{41}$$

In Ω_1^-, the application of the Green's second identify to ϕ_1^- and ψ_1^- leads to

$$\iint_{S_{1,b}^{-} \cup S_{1,d}^{-} \cup S_{1,f}^{-}} \left(\phi_1^{-} \frac{\partial \psi_1^{-}}{\partial n} - \psi_1^{-} \frac{\partial \phi_1^{-}}{\partial n} \right) ds = 0, \tag{42}$$

in which, $S_{1,b}^-$ is the inner wall surface of the real cylinder; $S_{1,d}^-$ and $S_{1,f}^-$ represent the seabed and free surface in Ω_1^-. Eq. (42) is also true when replacing ϕ_1^- with ϕ_I. That is

$$\iint_{S_{1,b}^{-} \cup S_{1,d}^{-} \cup S_{1,f}^{-}} \left(\phi_I \frac{\partial \psi_1^{-}}{\partial n} - \psi_1^{-} \frac{\partial \phi_I}{\partial n} \right) ds = 0. \tag{43}$$

After introducing the seabed and free surface boundary conditions satisfied by ψ_1^-, ϕ_1^- and ϕ_I, Eqs. (42) and (43) can be reduced to

$$\iint_{S_{1,b}^{-}} \left(\phi_1^{-} \frac{\partial \psi_1^{-}}{\partial r} - \psi_1^{-} \frac{\partial \phi_1^{-}}{\partial r} \right) ds = 0, \tag{44}$$

and

$$\iint_{S_{1,b}^{-}} \left(\phi_I \frac{\partial \psi_1^{-}}{\partial r} - \psi_1^{-} \frac{\partial \phi_I}{\partial r} \right) ds = 0. \tag{45}$$

By combining Eqs. (41), (44) and (45) and making use of Eqs. (5) and (27), we can obtain

$$-\int_{-d}^{0}\int_{0}^{2\pi} \left(\phi^{+} - \phi_1^{-} \right)\Big|_{r_1=a_1} u_1(\theta_1) a_1 dz_1 d\theta_1 = \int_{-d}^{0}\int_{0}^{2\pi} \left(\psi^{+} - \psi_1^{-} \right) \frac{\partial \phi_I}{\partial r}\bigg|_{r_1=a_1} a_1 dz_1 d\theta_1. \tag{46}$$

After some arrangements, the difference between the auxiliary radiation potential across the porous wall can be expressed as

$$\left(\psi^{+} - \psi_1^{-} \right)\Big|_{r_1=a_1} = -\sum_{m=-\infty}^{+\infty} \left\{ \frac{2i\hat{A}_{m,0}^{1}}{\pi\kappa_0 a_1 J_m'(\kappa_0 a_1)} Z_0(\kappa_0 z_1) - \sum_{l=1}^{\infty} \frac{\hat{A}_{m,l}^{1}}{\kappa_l a_1 I_m'(\kappa_l a_1)} Z_l(\kappa_l z_1) \right\} e^{im\theta_1}. \tag{47}$$

To distinguish the radiation potentials related to different motions, hereinafter the symbols $\hat{A}_{x,m,l}^{j}$ and $\hat{A}_{y,m,l}^{j}$ are used to represent the coefficients associated with the out-of-phase surge motions and the in-phase sway motions respectively. By substituting Eqs. (10) and (47) into Eq. (46) and utilizing the orthogonal property of sin$m\theta$, cos$m\theta$

and the vertical eigenfunctions, we can obtain that

$$\begin{Bmatrix} f_x \\ f_y \end{Bmatrix} = 4\omega\rho N_0\left(\kappa_0 d\right) \sum_{m=-\infty}^{+\infty} \begin{Bmatrix} \hat{A}^1_{x,\,-m,\,0} \\ \hat{A}^1_{y,\,-m,\,0} \end{Bmatrix} \Lambda^1_m \left(-1\right)^m, \tag{48}$$

in which $N_0\left(\kappa_0 d\right)$ represents the inner products of $Z_0\left(\kappa_0 z_1\right)$ and is given by

$$N_0\left(\kappa_0 d\right) = \frac{2\kappa_0 d + \sinh 2\kappa_0 d}{4\kappa_0 \cosh^2 \kappa_0 d}. \tag{49}$$

From Eq. (48), it can be noted that the evanescent modes of the auxiliary radiation potential make no contribute to wave force. Eq. (48) relates the wave force on the cylinder near a vertical wall to the propagation modes of radiation waves due to the motion of the cylinder. Now an alternative model for the evaluation of wave force is developed.

6. Convergence test and validation

In the previous sections, two different analytical models have been developed for the evaluation of wave force on a porous cylinder located in front of a vertical wall. Hereinafter, the factor $\rho g a^2 A$ is used to nondimensionalize the wave force. From Eqs. (24) and (48), it is clearly observed that the convergence of wave force from both the two models depends on the number of Fourier modes. In the numerical algorithm, totally $2M + 1$ Fourier modes (from order $-M$ to order M) have been considered. To check the convergence characteristics of the present solution with respect to the number of Fourier modes, calculations are performed for the case of $d/a = 5$, $e/a = 1$, $\beta = \pi/4$ and $|G_0| = 1$. Tables 1 and 2 list the dimensionless wave force based on the two models as a function of M for different wave frequencies. In these tables, the results referred as 'Direct' and 'Indirect' are obtained according to Eqs. (24) and (48), respectively. By inspecting the results listed in Tables 1 and 2, the two models both possess good convergence characteristics. It can be concluded that the use of 21 Fourier modes (M = 10) is sufficient to ensure 4 significant decimals of accuracy and M = 10 is adopted in all subsequent computations. Meanwhile, in order to confirm the validity of the present solution, a comparison between the results based on the two models is made.

Comparison confirms the good agreement. With the same value of M, the two models can give almost the same results.

Table 1 Convergence test on the dimensionless wave force, $|f_x/(\rho g a^2 A)|$, on a porous cylinder in front of a vertical wall with varying M ($e/a = 1$, $\beta = \pi/4$, $|G_0| = 1$ and $d/a = 5$)

$\kappa_0 a =$	0.5		1.0		1.5		2.0	
$M =$	Direct	Indirect	Direct	Indirect	Direct	Indirect	Direct	Indirect
2	3.6076	3.6076	2.0693	2.0693	0.6360	0.6360	0.1286	0.1286
3	3.6081	3.6081	2.0730	2.0730	0.6296	0.6296	0.1284	0.1284
5	3.6081	3.6081	2.0730	2.0730	0.6297	0.6297	0.1268	0.1268
10	3.6081	3.6081	2.0730	2.0730	0.6297	0.6297	0.1268	0.1268
20	3.6081	3.6081	2.0730	2.0730	0.6297	0.6297	0.1268	0.1268

Table 2 Convergence test on the dimensionless wave force, $|f_y/(\rho g a^2 A)|$, on a porous cylinder in front of a vertical wall with varying M ($e/a = 1$, $\beta = \pi/4$, $|G_0| = 1$ and $d/a = 5$)

$\kappa_0 a =$	0.5		1.0		1.5		2.0	
$M =$	Direct	Indirect	Direct	Indirect	Direct	Indirect	Direct	Indirect
2	3.9726	3.9726	0.2908	0.2908	0.3994	0.3994	0.2655	0.2655
3	3.9719	3.9719	0.2906	0.2906	0.4015	0.4015	0.2624	0.2624
5	3.9719	3.9719	0.2906	0.2906	0.4015	0.4015	0.2624	0.2624
10	3.9719	3.9719	0.2906	0.2906	0.4015	0.4015	0.2624	0.2624
20	3.9719	3.9719	0.2906	0.2906	0.4015	0.4015	0.2624	0.2624

To provide a further check on the validity of the present solution, a comparison with the published results from Teng and Ning (2003), which were obtained based on the boundary element method, is made. The case that the incident wave acts on an impermeable vertical cylinder ($|G_0| = 0$) in front of a vertical wall is concerned in the comparison. Fig. 3 illustrates the dimensionless wave force corresponding to $e/a = 1$ and $d/a = 1$. As the two developed models give almost the same predictions, only those based on Eq. (24) are presented in Fig. 3. From the comparison shown in Fig. 3, it can be observed that a good agreement is achieved, which further confirms the validity of the present solution.

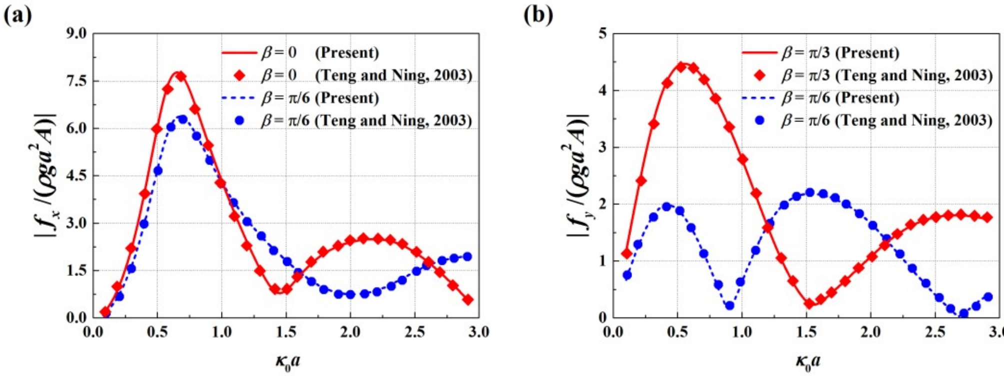

Fig. 3 Comparison of the dimensionless wave force on a vertical cylinder in front of a vertical wall (e/a = 1, $|G_0|$ = 0 and d/a = 1)

7. Results and discussions

With the validation of the present solution, a detailed parametric study concerning a porous cylinder in front of a wall is performed in which the effects of the porous parameter G_0, the distance between the cylinder and the wall e and the incident wave heading β on the wave force, wave runup and wave elevation distribution around the cylinder are investigated. The extension of our model to the case of a cylinder array has also been performed. Numerical results related to an array of porous cylinders in front of a wall are also presented. In all the subsequent calculations, the water depth keeps constant at $d/a = 5$.

7.1 Wave force a porous cylinder in front of a wall

The effects of the distance between the cylinder and the wall e on the wave force acting on the cylinder are shown in Fig. 4. The dimensionless wave force is plotted versus the dimensionless wave number $\kappa_0 a$ in the cases of varying values of e and a constant incident wave heading β = 0. In order to get a better understanding, the situation that a cylinder is placed in unbounded water is also considered and the results referred as 'UW' are corresponding to this situation. In addition, the results shown in Fig. 4 are corresponding to different porous effect parameters which are varied as $|G_0|$ = 0.0, 0.25, 0.5, 0.75 and 1.0. From Fig. 4, it is noted that the influence of G_0 is very evident and the wave force acting on a porous cylinder are obviously reduced, compared with those acting on an impermeable cylinder ($|G_0| = 0|$). By comparing the results for different values of e, it is noted that the wave force experienced by a cylinder in front of a wall behaves an oscillation around that acting on a cylinder placed in unbounded water. The oscillation of the wave force with $\kappa_0 a$ is found to depend on the distance between the cylinder and the wall. The larger the value of e is, the more frequently the wave force oscillates with $\kappa_0 a$. When a cylinder is placed in the unbounded water (see Fig. 4d), the behavior of the results with $|G_0| > 0$ is different from that with $|G_0| = 0$ and there exists an obvious zero-excitation frequency at which the structure endures no wave force. This is mainly due to the cancellation between the wave action on outer and inner wall surfaces of the porous cylinder. The obvious zero-excitation frequency can also be observed when a porous cylinder is placed in the bounded water (see Figs. 4a, 4b and 4c).

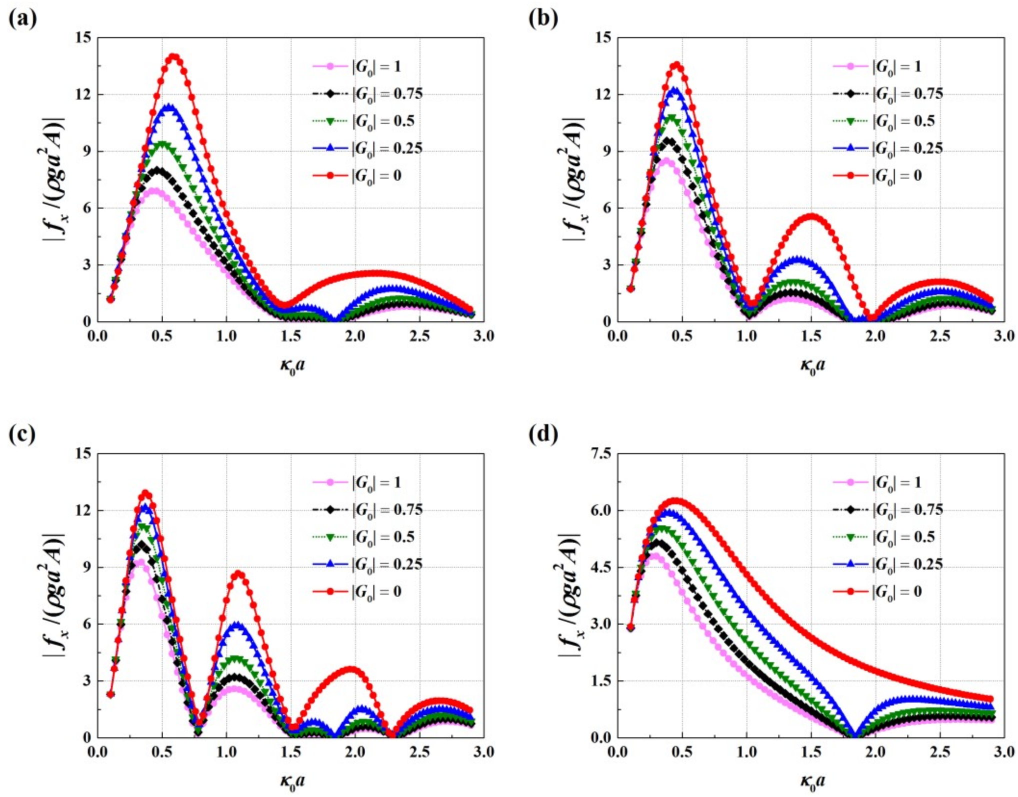

Fig. 4 Magnitude of the dimensionless wave force on a porous cylinder in front of a wall for different values of $|G_0|$ with $\beta = 0$ and $d/a = 5$ (a) $e/a = 1$ (b) $e/a = 2$ (c) $e/a = 3$ (d) UW

The influence of the wave heading β on the wave force is illustrated in Fig. 5 with e and $|G_0|$ fixed at $2a$ and 1, respectively. Meanwhile, the incident wave heading is varied as β/π = 1/16, 1/8, 3/16 and 1/4. Each curve in Fig. 5 is characterized by an obvious peak in the low frequency region. For the wave force components in the x- and y-directions, this obvious peak is gradually amplified and reduced, respectively, as β increases, which is attributed to the changes in the projection area of wave action. Besides the obvious peak, small oscillations can be found in the high frequency region. The peak frequencies of these small oscillations move gradually to the high frequency region as β increases.

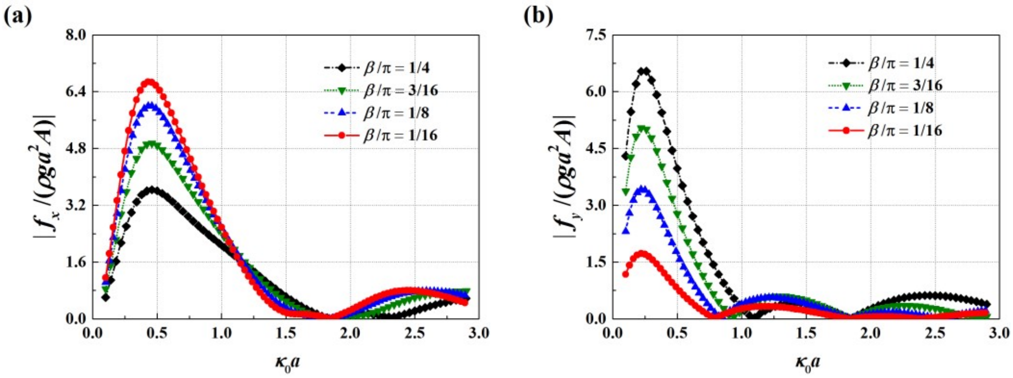

Fig. 5 Magnitude of the dimensionless wave force on a porous cylinder in front of a wall for different values of β with e/a = 1, $|G_0|$ = 1 and d/a = 5 (a) $|f_x/(\rho g a^2 A)|$ (b) $|f_y/(\rho g a^2 A)|$

7.2 Wave runup along a porous cylinder in front of a wall

Numerical studies on the wave elevation along the outer and inner wall surface of the porous cylinder, also known as wave runup, at three points called P_1, P_2 and P_3, are performed in this subsection. The coordinates of the feature points P_1, P_2 and P_3 in the xoy plane are $(-e, 0)$, $(-e-a, -a)$ and $(-e-2a, 0)$, respectively. The definition of P_1, P_2 and P_3 can also be found in Fig. 1. Hereinafter, the incident wave amplitude A is used to nondimensionalize the wave runup.

The variation of the wave runup at P_1, P_2 and P_3 on the outer and inner wall surface of the cylinder is plotted versus $\kappa_0 a$ in Figs. 6 and 7 with β = 0 and e/a = 1. In these calculations, the magnitude of the porous parameter is varied as $|G_0|$ = 0, 0.25, 0.5, 0.75

and 1. The hydrodynamic pressure along the waterline is directly proportional to the wave elevation. As a result, it can be noted that the changing trend of the wave runup is similar to that of wave force, which behaves oscillation with $\kappa_0 a$. The effects of the porous parameter on the wave runup is obvious. On the outer wall surface, the peak value in general decreases with increasing $|G_0|$, especially when $|G_0| < 0.5$. Meanwhile, an increase in $|G_0|$ can cause an increase in the wave transmission through the porous wall. The changing trend and magnitude of the wave runup on the inner wall gradually coincide with that on the outer wall as $|G_0|$ increases.

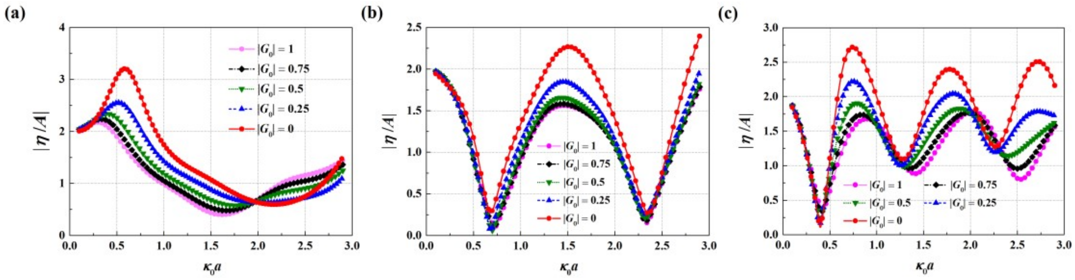

Fig. 6 Magnitude of the dimensionless wave runup on the outer wall surface of a porous cylinder in front of a wall with e/a = 1, β = 0 and d/a = 5 (a) P_1 (b) P_2 (c) P_3

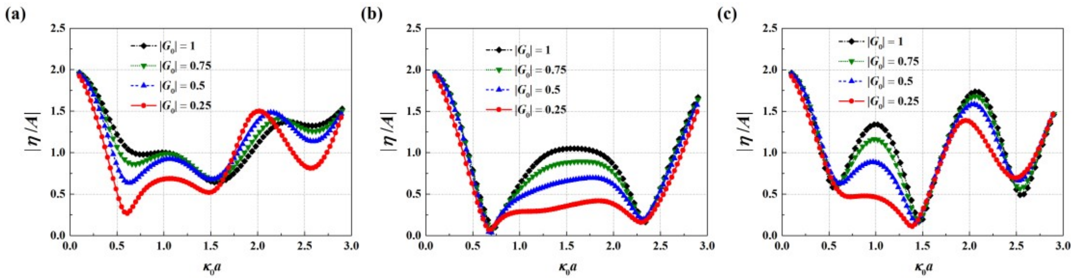

Fig. 7 Magnitude of the dimensionless wave runup on the inner wall surface of a porous cylinder in front of a wall with e/a = 1, β = 0 and d/a = 5 (a) P_1 (b) P_2 (c) P_3

Figs. 8-9 show the wave runup at the three points corresponding to e/a = 1, 2, 3 and unbounded water condition with β and $|G_0|$ fixed at 0 and 1, respectively. The waves reflected from the wall can cause obvious disturbance on the wave field around the cylinder, leading to the intensive oscillation of the wave runup with increasing $\kappa_0 a$. Obvious amplification or reduction of the wave runup can be induced when the effects from the wall are considered. The wave runup with e/a = 1, 2 and 3 oscillates around that experienced by a cylinder in unbounded water. At P_1, which is closest to the vertical wall among the three locations, the wave runup oscillates less frequently with $\kappa_0 a$ when compared with that at other locations. Meanwhile, such oscillation also depends on the distance between the cylinder and the wall. As e increases, the wave runup oscillates more frequently with $\kappa_0 a$.

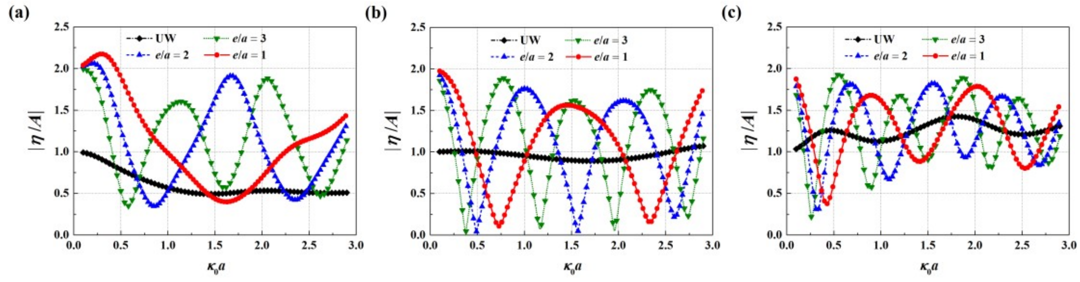

Fig. 8 Magnitude of the dimensionless wave runup on the outer wall surface of a porous cylinder in front of a wall for different values of e with $\beta = 0$, $|G_0| = 1$ and $d/a = 5$ (a) P_1 (b) P_2 (c) P_3

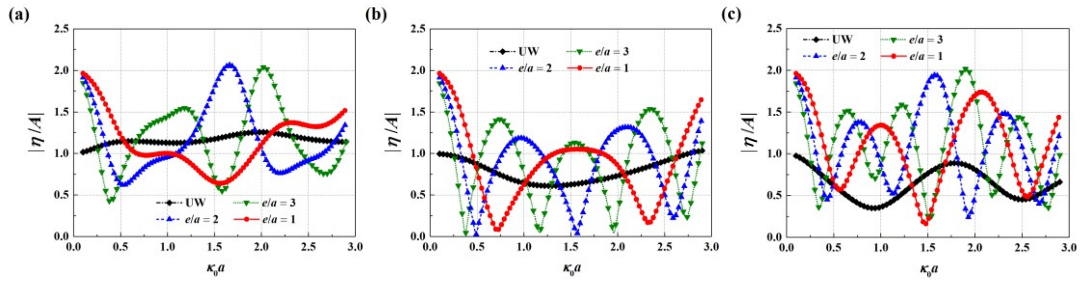

Fig. 9 Magnitude of the dimensionless wave runup on the inner wall surface of a porous cylinder in front of a wall for different values of e with $\beta = 0$, $|G_0| = 1$ and $d/a = 5$ (a) P_1 (b) P_2 (c) P_3

Figs. 10 and 11 present the wave runup for different cases of incident wave headings with e and $|G_0|$ fixed at $2a$ and 1, respectively. The effects of the incident wave heading β can then be investigated. As β gradually increases to $\pi/2$, the two incident waves in the imaginary system are gradually merged into one. In the meantime, the phase difference between the individual contribution from the two waves to the wave field gradually decreases. As a result, it is observed that the oscillation of the wave runup with $\kappa_0 a$ becomes less intensive as β increases.

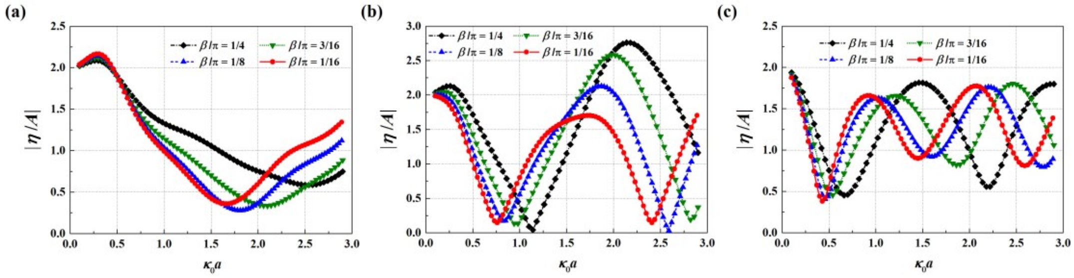

Fig. 10 Magnitude of the dimensionless wave runup on the outer wall surface of a porous cylinder in front of a wall for different values of β with e/a = 1, $|G_0|$ = 1 and d/a = 5 (a) P_1 (b) P_2 (c) P_3

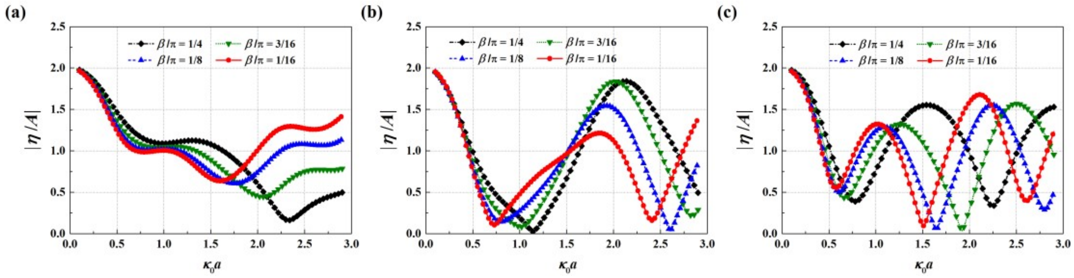

Fig. 11 Magnitude of the dimensionless wave runup on the inner wall surface of a porous cylinder in front of a wall for different values of β with e/a = 1, $|G_0|$ = 1 and d/a = 5 (a) P_1 (b) P_2 (c) P_3

7.3 Wave elevation in the vicinity of a porous cylinder in front of a wall

The dimensionless wave elevation in the vicinity of a porous cylinder in front of a wall under normal wave incidence (β = 0) is shown in Figs. 12 and 13 for $\kappa_0 a$ = 0.74, 0.61 and 0.52 corresponding to e/a = 1, 2 and 3, respectively. In addition, Figs. 12 and 13 correspond to the cases of an impermeable cylinder ($|G_0|$ = 0) and a porous cylinder with $|G_0|$ = 1, respectively. From Fig. 12, alternative occurrence of peaks and troughs can be observed along the direction of wave propagation. Under the three combinations of $\kappa_0 a$ and e/a, significant wave runup can be observed around the weather side of an impermeable cylinder (see Fig. 12). Meanwhile, such significant amplification in the wave runup can be obviously suppressed when making the cylinder porous (see Fig. 13), demonstrating the dramatic effects of the porosity of the cylinder.

To further emphasize the variation in the wave elevation, a section across the domain through the center of the cylinder (y = 0) is considered. The wave elevation along y = 0 with β = 0 is given in Fig. 14 for the three combinations of $\kappa_0 a$ and e/a as discussed in Figs. 12 and 13. In Fig. 14, the value of $|G_0|$ is varied between 0 and 1 with an interval of 0.25. As the waves cannot enter through an impermeable cylinder and hence for the case of $|G_0| = 0$ the wave elevation inside the cylinder is not given. It is evident from Fig. 14 that an increase in $|G_0|$ can lead to a decrease in the wave runup around both the weather side and lee side outside the cylinder. For the first combination of $\kappa_0 a$ and e/a (see Fig. 14a), the wave elevation inside the cylinder in general increases as $|G_0|$ increases at each location along $y = 0$. Meanwhile, for other combinations (see Figs. 14(b) and 14(c)), the wave runup around the weather side inside the cylinder has an increase trend with the increase of $|G_0|$, whereas around the lee side inside the cylinder the effects of $|G_0|$ on the wave runup are not evident.

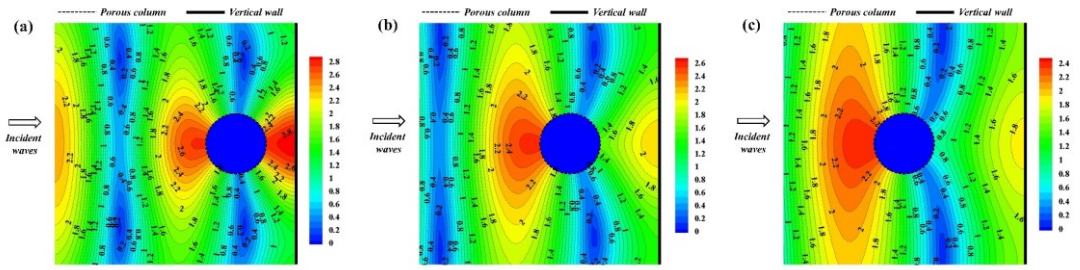

Fig. 12 Magnitude of the dimensionless wave elevation in the vicinity of a porous cylinder in front of a wall with $|G_0| = 0$, $\beta = 0$ and $d/a = 5$ (a) $\kappa_0 a = 0.74$, $e/a = 1$ (b) $\kappa_0 a = 0.61$, $e/a = 2$ (c) $\kappa_0 a = 0.52$, $e/a = 3$

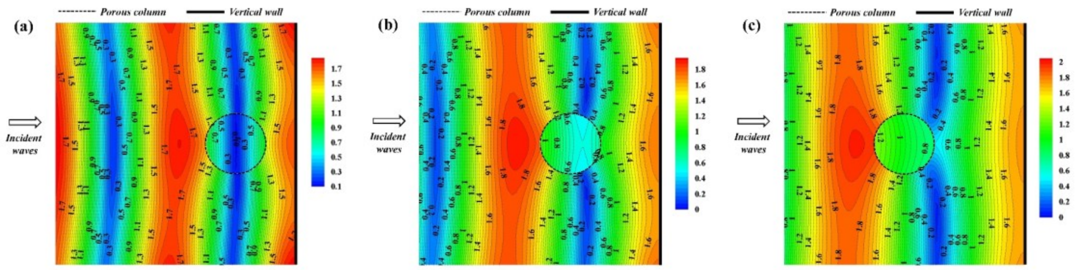

Fig. 13 Magnitude of the dimensionless wave elevation in the vicinity of a porous cylinder in front of a wall with $|G_0| = 1$, $\beta = 0$ and $d/a = 5$ (a) $\kappa_0 a = 0.74$, $e/a = 1$ (b) $\kappa_0 a = 0.61$, $e/a = 2$ (c) $\kappa_0 a = 0.52$, $e/a = 3$

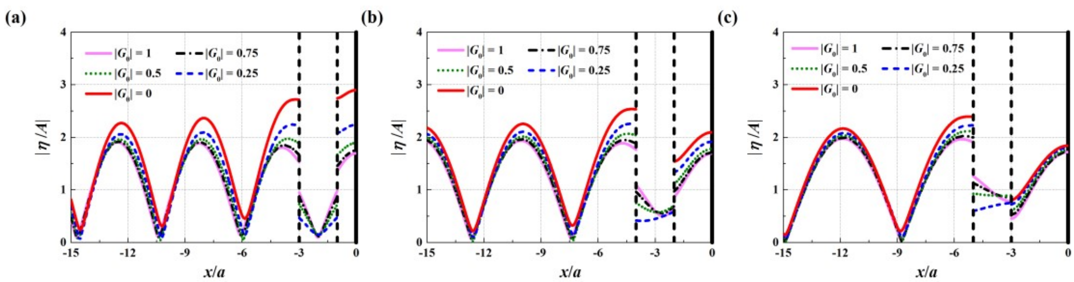

Fig. 14 Magnitude of the dimensionless free-surface elevation along y = 0 for different values of $|G_0|$ with β = 0 and d/a = 5 (a) $\kappa_0 a$ = 0.74, e/a = 1 (b) $\kappa_0 a$ = 0.61, e/a = 2 (c) $\kappa_0 a$ = 0.52, e/a = 3

The dimensionless wave elevation in the vicinity of the cylinder with β/π = 1/4 and $|G_0|$ = 1 is plotted in Fig. 15 for the three combinations of $\kappa_0 a$ and e/a as discussed above. Fig. 15 is characterized by the alternative occurrence of peaks and troughs, which is similar to the observation in Figs. 12 and 13. Meanwhile, with β/π = 1/4, the wave field losses the character of symmetry. Furthermore, it is noted that an increase of β/π from 0 to 1/4 can cause a shift in the location where the peaks and troughs occur. To further reveal the phase shift of the wave elevation with the increase of wave obliqueness, the free-surface elevation along y = 0 with $|G_0|$ = 1 is given in Fig. 16 for the three combinations of $\kappa_0 a$ and e/a. In Fig. 16, the value of β/π is ranged from 1/16 to 1/4 with an interval of 1/16. It is observed that the peaks and troughs inside and outside the cylinder both obviously move to the upstream region as the wave obliqueness increases.

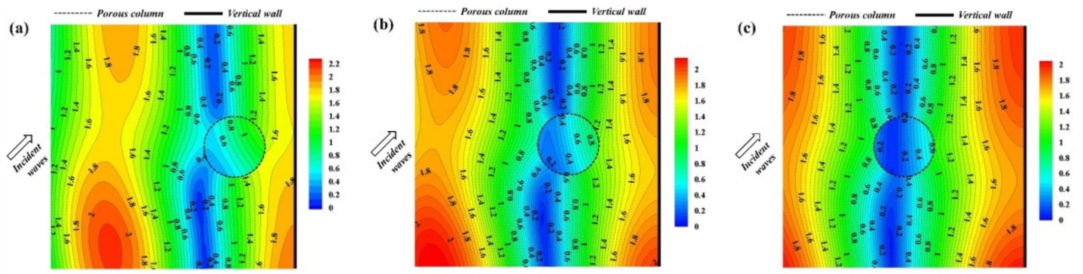

Fig. 15 Magnitude of the dimensionless wave elevation in the vicinity of a porous cylinder in front of a wall with $|G_0|$ = 1, β = π/4 and d/a = 5 (a) $\kappa_0 a$ = 0.74, e/a = 1 (b) $\kappa_0 a$ = 0.61, e/a = 2 (c) $\kappa_0 a$ = 0.52, e/a = 3

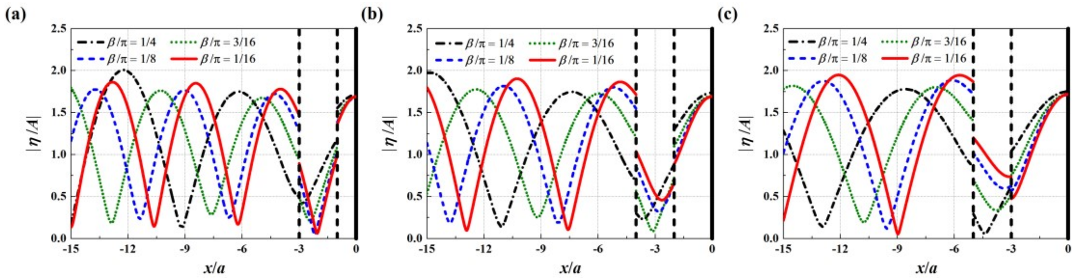

Fig. 16 Magnitude of the dimensionless wave elevation in the vicinity of the cylinder with $|G_0|$ = 1, β = π/4 and d/a = 5 (a) $\kappa_0 a$ = 0.74, e/a = 1 (b) $\kappa_0 a$ = 0.61, e/a = 2 (c) $\kappa_0 a$ = 0.52, e/a = 3

7.4 Wave interaction with an array of porous cylinders in front of a wall

We consider the wave interaction with an array of porous cylinders in front of a wall. The cylinders in the array are numbered as $j = 1, 2, \ldots, C_0, \ldots, N_b$. After updating the number of the cylinders in front of the wall, N_b, and the location and radius of each cylinder, this problem can be tackled following the solution procedure presented in Section 3. In addition, the method based on the introduction of auxiliary radiation potential can also be used to evaluate the wave force on a specific cylinder in the array, such as cylinder C_0. In this method, the radiation potential due to the harmonic oscillation of cylinder C_0 in specific directions is required. Based on the image principle, the wave radiation problem in bounded water can be transformed to the equivalent one in open seas. In the imaginary system in open seas, besides the array of N_b real cylinders, there is also an array of N_b image cylinders. The real and the image cylinders are symmetrical to the original vertical wall. The equivalent radiation problem in open seas is due to the motions of the cylinder C_0 and its symmetrical cylinder. After obtaining the radiation potential, the application of the Green's second identify to the diffraction potential and the auxiliary radiation potential in the region inside and outside the cylinder array, respectively, in the orginal bounded watre can give the alternative solution of wave force. The alternative solution relates the wave force on cylinder C_0 to the propagation modes of radiation waves outside the cylinder array due to the motion of cylinder C_0. In this section, the cases of $N_b = 2$, 3 and 5 are concerned and the corresponding layout of the cylinder array is given in Fig. 17. As shown in Fig. 17, the cylinders, each having a radius a about its vertical axis, are equally spaced and lined up in a row parallel to the wall. The axes of adjacent cylinders are separated by a distance of $4a$. When $N_b = 2$, the lower cylinder is numbered as C_0 (see Fig. 17a). When $N_b = 3$ and 5, the middle cylinder in the array is numbered as C_0 (see Figs. 17b and 17c). In addition, the normal wave incidence ($\beta = 0$) is primarily concerned in the following calculation.

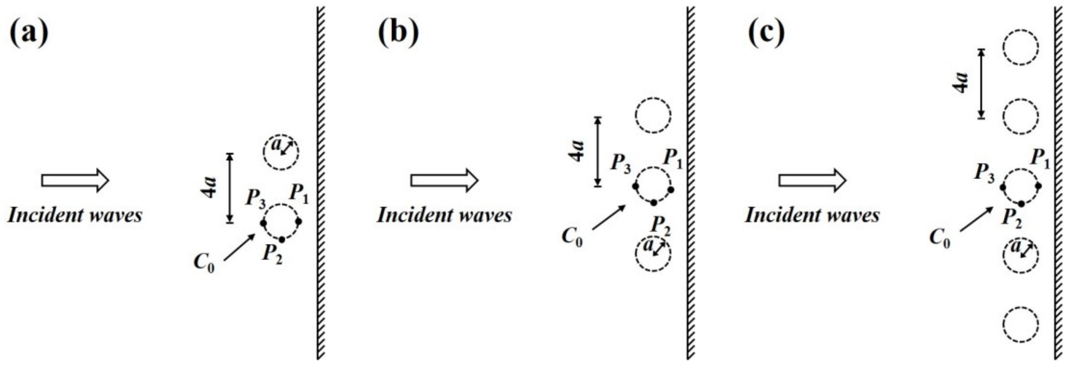

Fig. 17 Definition sketches for an array of porous cylinders in front of a wall (a) $N_b = 2$ (b) $N_b = 3$ (c) $N_b = 5$

Fig. 18 shows the wave force experienced by the cylinder C_0 in the array of porous cylinders with $|G_0| = 0$ and the distance between the cylinder and the wall varies as $e/a = 1$, 2 and 3. The results corresponding to a single cylinder ($N_b = 1$) and a cylinder array ($N_b = 2$, 3 and 5) are both shown in Fig. 18 for the purpose of comparison. From Fig. 18, it is observed that the wave force on a cylinder in an array can follow a similar changing trend to that on a single cylinder. However, small oscillations riding on the results for $N_b = 1$ can be observed in the results for $N_b = 2$, 3 and 5, which is due to the interference effects between adjacent cylinders. Analogous results to those in Fig. 18 but with $|G_0| = 1$ are shown in Fig. 19. When $|G_0| > 0$, the wave transmission through the porous wall of the cylinder can occur, which can weaken the interference effects between adjacent cylinders. As a result, when $|G_0| = 1$, the results corresponding to different values of N_b are in better agreement.

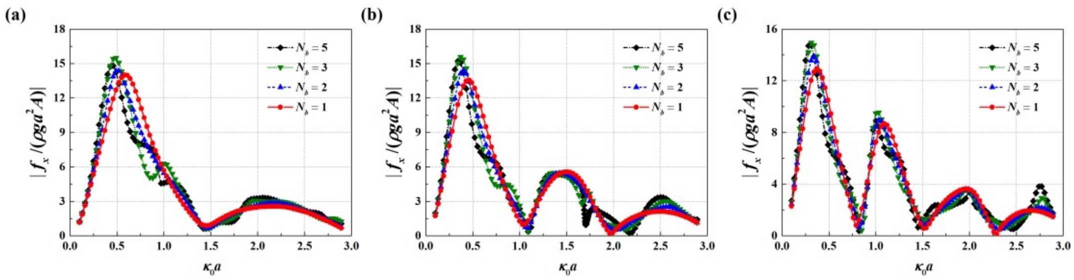

Fig. 18 Magnitude of the dimensionless wave force on the cylinder C_0 in an array of porous cylinders with $|G_0| = 0$, $\beta = 0$ and $d/a = 5$ (a) $e/a = 1$ (b) $e/a = 2$ (c) $e/a = 3$

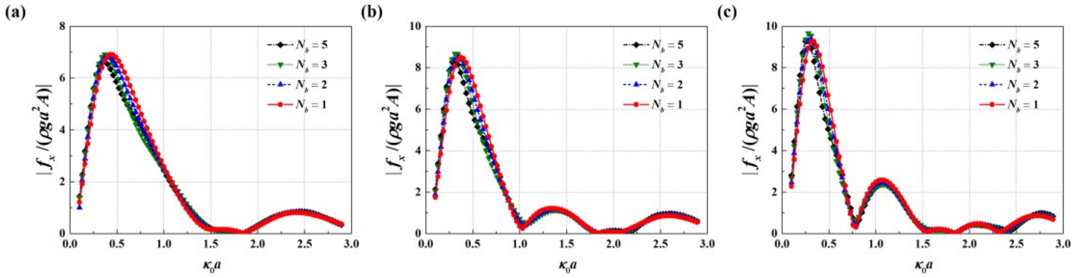

Fig. 19 Magnitude of the dimensionless wave force on the cylinder C_0 in an array of porous cylinders with $|G_0| = 1$, $\beta = 0$ and $d/a = 5$ (a) $e/a = 1$ (b) $e/a = 2$ (c) $e/a = 3$

Fig. 20 shows the variation of wave runup at P_1, P_2 and P_3 on the outer wall surface of porous cylinder in the array with $e/a = 1$ and $|G_0| = 0$. When $N_b = 2$, 3 and 5, the definition of P_1, P_2 and P_3 can be found in Fig. 17. As shown in Fig. 20, the wave runup on a porous cylinder in an array oscillates more intensively with $\kappa_0 a$ than that on a single cylinder. After placing a cylinder in an array, obvious reinforcement and diminishment of the wave runup can be induced, resulting from the constructive and destructive interferences between adjacent cylinders. Figs. 21 and 22 show the variation of wave runup at P_1, P_2 and P_3 on the outer and inner wall surfaces of porous cylinder in the array with $e/a = 1$ and $|G_0| = 1$. It is noted that the wave runups corresponding to different layouts of the cylinder array with $|G_0| = 1$ are much closer to each other when compared with those with $|G_0| = 0$, which suggests that the porous effects can obviously weaken the interference effects between adjacent cylinders.

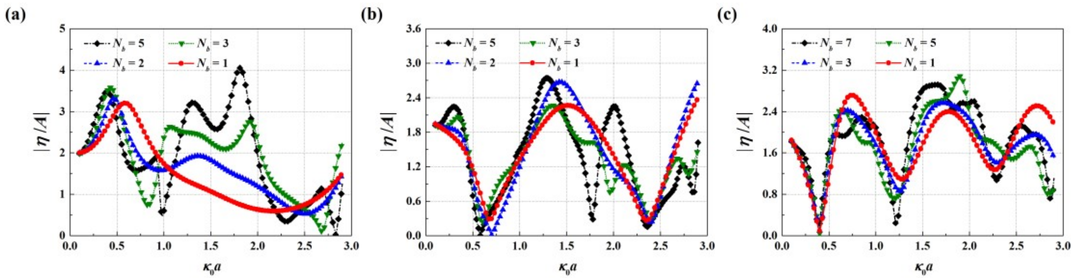

Fig. 20 Magnitude of the dimensionless wave runup on the outer wall surface of a porous cylinder in an array with $e/a = 1$, $|G_0| = 0$, $\beta = 0$ and $d/a = 5$ (a) P_1 (b) P_2 (c) P_3

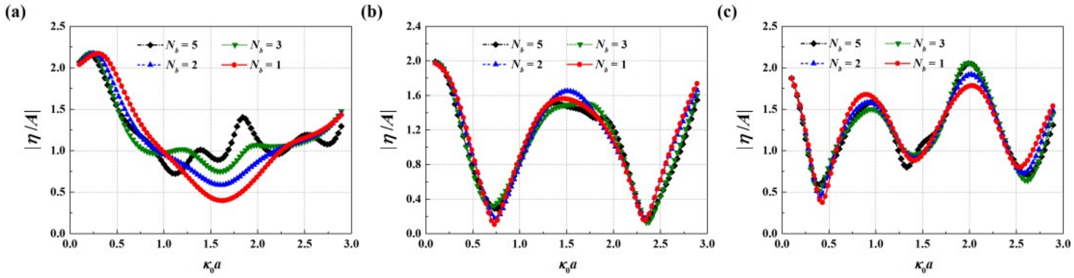

Fig. 21 Magnitude of the dimensionless wave runup on the outer wall surface of a porous cylinder in an array with e/a = 1, $|G_0|$ = 1, β = 0 and d/a = 5 (a) P_1 (b) P_2 (c) P_3

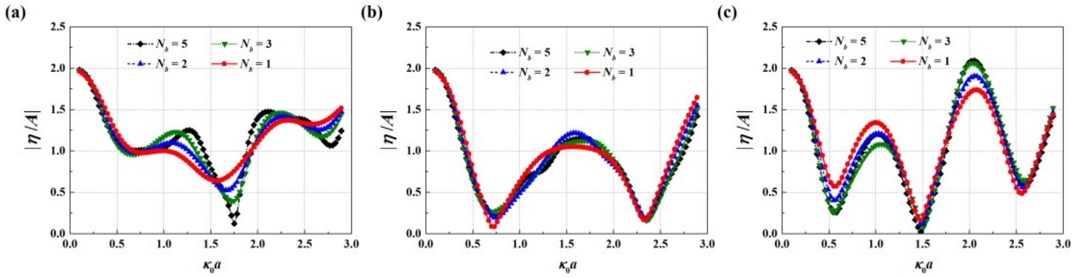

Fig. 22 Magnitude of the dimensionless wave runup on the inner wall surface of a porous cylinder in an array with e/a = 1, $|G_0|$ = 1, β = 0 and d/a = 5 (a) P_1 (b) P_2 (c) P_3

The dimensionless wave elevation in the vicinity of an array of porous cylinders is shown in Fig. 23 with e/a = 1 and $|G_0|$ = 0 for $\kappa_0 a$ =0.69, 0.64 and 0.84 corresponding to N_b = 2, 3 and 5, respectively. Analogous results to those in Fig. 23 but with $|G_0|$ = 1 are shown in Fig. 24. In Fig. 23, significant peaks can be observed in the upstream region in front of the cylinder array. Meanwhile, the appearance of those large peaks is obviously suppressed after making the cylinders porous (see Fig. 24), which demonstrates the remarkable porous effect of the cylinders on the wave elevation distribution.

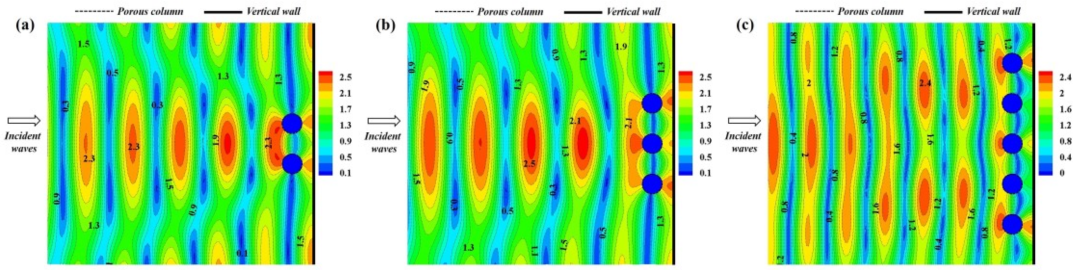

Fig. 23 Magnitude of the dimensionless wave elevation in the vicinity of an array of porous cylinders in front of a wall with e/a = 1, $|G_0|$ = 0, β = 0 and d/a = 5 (a) $\kappa_0 a$ = 0.69, N_b = 2 (b) $\kappa_0 a$ = 0.64, N_b =

3 (c) $\kappa_0 a = 0.84$, $N_b = 5$

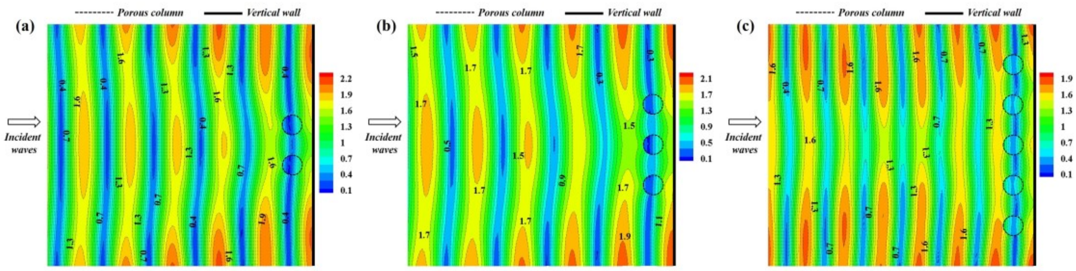

Fig. 24 Magnitude of the dimensionless wave elevation in the vicinity of an array of porous cylinders in front of a wall with $e/a = 1$, $|G_0| = 1$, $\beta = 0$ and $d/a = 5$ (a) $\kappa_0 a = 0.69$, $N_b = 2$ (b) $\kappa_0 a = 0.64$, $N_b = 3$ (c) $\kappa_0 a = 0.84$, $N_b = 5$

8. Conclusion

The interaction of water wave with a bottom-mounted surface-piercing porous cylinder, located at a finite distance from a rigid vertical wall, is studied in the framework of potential flow theory. To carry out the study, a new analytical model is developed, and by introducing an auxiliary radiation potential a new alternative method to calculate the wave force is also proposed. The main conclusions of this study are summarized as follows:

(1) By undertaking a convergence test, the sensitivity of the present model to the number of Fourier modes is investigated. Two approaches have been developed in this study for the calculation of wave force. One approach is based on the explicit solution of velocity potential. The Haskind-Hanaoka relation, which has been extended to the case of a porous structure in Zhao et al. (2011), is applied in the other approach. It is noted that the two approaches both possess good convergence and the results based on them agree well with each other. In addition, for the case of an impermeable cylinder situated near a vertical wall, the present results agree well with those reported in previous studies.

(2) In the two approaches developed for the calculation of wave force, the wave diffraction and radiation problems related to a pours cylinder in front of a wall have

been solved, respectively. The image principle is used to transfer the original diffraction or radiation problem in bounded water into the equivalent one in open seas. In the equivalent problem, simple relationships between the Fourier coefficients related to the real and image cylinders have been established, based on which the no-flow condition on the vertical wall is demonstrated.

(3) The waves reflected from the vertical wall can obviously disturb the wave field near the cylinder, leading to that the wave force acting on a cylinder in front of a wall behaves oscillation around that experienced by a cylinder placed in unbounded water. The wave force can be remarkably amplified at specific frequencies due to the effects of the vertical wall. Meanwhile, such obviously amplified wave force can be apparently reduced on the porous cylinder. Regarding the porous effects, the wave force continues to decrease as the porosity increases.

(4) The presence of the fully-reflective vertical wall can lead to obvious oscillation of the wave runup with respect to the wave frequency. The oscillation in the wave runup depends on the spacing between the cylinder and the wall. The larger the spacing is, the more frequently the wave runup oscillates with the wave frequency. It is found that the obvious amplification in the wave runup can be effectively suppressed on the porous cylinder. Meanwhile, an increase of the porous effect parameter can cause an increase of the wave transmission through the porous wall. Correspondingly, the changing trend and magnitude of the wave runup on the inner and outer wall surfaces of the cylinder gradually coincide with each other. It is also found that the wave obliqueness can obviously affect the wave elevation distribution around the cylinder. As the wave obliqueness increases, the locations where peaks and troughs occur obviously move to the upstream region.

(5) The extension of our model to the case of a cylinder array in front of a wall has been performed. Under normal incidence, the wave interaction with an array of porous cylinders in front of a wall has been investigated. The porous cylinders in the array are aligned in a straight line and equally spaced. It is noted that the porous effects of the cylinder can obviously weaken the interference effects between adjacent cylinders. As

the porosity increases, the wave force and runup on a porous cylinder in an array near a wall can gradually coincide with those on a single porous cylinder near a wall.

Appendix: No-flow condition at the wall in the imaginary system

Here, it will be shown that the no-flow condition at the wall is satisfied in the imaginary system (see Fig. 2).

In Fig. 2, the two symmetrical cylinders in open seas are under the action of two plane incident waves of amplitude A and frequency ω propagating in the directions β and $\pi - \beta$, respectively. In the exterior region Ω^+, the velocity potential ϕ^+ can be expressed as a sum of the incident and diffraction potentials. With the application of Eqs. (6), (8) and (13), it can be obtained that

$$\phi^+ = -\frac{iAg}{\omega} Z_0(\kappa_0 z) e^{i\kappa_0 y \sin\beta}\left(e^{i\kappa_0 x\cos\beta} + e^{-i\kappa_0 x\cos\beta}\right) + \sum_{j=1}^{N=2}\sum_{m=-\infty}^{+\infty} A_m^j C_m^j H_m(\kappa_0 r_j) Z_0(\kappa_0 z_j) e^{im\theta_j}. \quad \text{(A1)}$$

In the framework of potential flow theory, the fluid velocity can be determined according to the gradient of velocity potential. It leads to

$$\begin{aligned} u_x^+ &= -\frac{iAg}{\omega} Z_0(\kappa_0 z) e^{i\kappa_0 y\sin\beta} i\kappa_0 \cos\beta\left(e^{i\kappa_0 x\cos\beta} - e^{-i\kappa_0 x\cos\beta}\right) \\ &+ \sum_{j=1}^{2}\sum_{m=-\infty}^{+\infty} A_m^j C_m^j\left[\kappa_0 H_m'(\kappa_0 r_j)\cos\theta_j - imH_m(\kappa_0 r_j)\frac{\sin\theta_j}{r_j}\right] Z_0(\kappa_0 z_j) e^{im\theta_j}, \end{aligned} \quad \text{(A2)}$$

in which, u_x^+ is velocity component in the x-direction for a fluid particle in Ω^+. In Eq. (A2), the coefficients A_m^j can be determined by solving Eq. (20a). In Eqs. (A1) and (A2), j = 1, 2 are corresponding to the real and image cylinders respectively. As the centres of the real and image cylinders are located at (−R, 0, 0) and (R, 0, 0) on the mean free surface and the two symmetrical cylinders have the same radius, i.e., $a_1 = a_2 = a$, Eq. (20a) can be rewritten as

$$A_m^j p_m + \sum_{n=-M}^{+M} A_n^k q_{m,n}^{j,k} = o_m^{j,k}, \quad j,\ k = 1,\ 2 \text{ and } j \neq k, \quad \text{(A3)}$$

in which, the coefficients p_m, $q_{m,n}^{j,k}$ and $o_m^{j,k}$ can be expressed as

$$p_m = p_{-m} = 1 + \frac{2G_0}{\pi\kappa_0 a}\frac{1}{J_m'(\kappa_0 a)H_m'(\kappa_0 a)}; \quad \text{(A4a)}$$

$$q_{m,\,n}^{j,\,k}=q_{-m,\,-n}^{k,\,j}=\frac{J_m'\left(\kappa_0 a\right)}{H_m'\left(\kappa_0 a\right)}H_{n-m}\left(2\kappa_0 R\right)\left(-1\right)^m e^{\frac{1}{2}i\left[n(k-j+1)-m(j-k+1)\right]\pi};\tag{A4b}$$

$$o_m^{j,\,k}=o_{-m}^{k,\,j}=\frac{iAg}{\omega}\left[e^{-i(k-j)\kappa_0 R\cos\beta}e^{-im\beta}+e^{i(k-j)\kappa_0 R\cos\beta}e^{im\beta}\left(-1\right)^m\right]i^m.\tag{A4c}$$

With the application of Eq. (A4), it is noted that except the unknown coefficients, other coefficients involved in Eq. (A3) keep the same after replacing k, j, m and n by j, k, $-m$ and $-n$. That is

$$A_{-m}^k p_m+\sum_{n=-M}^{+M}A_{-n}^j q_{m,\,n}^{j,\,k}=o_m^{j,\,k},\quad j,\ k=1,\ 2\text{ and } j\neq k.\tag{A5}$$

Eqs. (A3) and (A5) suggest that the following relationship is held for A_m^j

$$A_m^j=A_{-m}^k,\quad j,\ k=1,\ 2\text{ and } j\neq k.\tag{A6}$$

At the wall (x = 0), the incident wave makes no contribution to u_x^+. If a location along the wall, with the coordinate (0, y_s, z_s) in the global coordinate system, is concerned, u_x^+ at this location can be expressed as

$$u_x^+=\sum_{m=-\infty}^{+\infty}\left(A_m^1-A_{-m}^2\right)\frac{J_m'\left(\kappa_0 a\right)}{H_m'\left(\kappa_0 a\right)}\left[\kappa_0 H_m'\left(\kappa_0 r_s\right)\cos\theta_s-imH_m\left(\kappa_0 r_s\right)\frac{\sin\theta_s}{r_s}\right]Z_0\left(\kappa_0 z_s\right)e^{im\theta_s},\tag{A7}$$

in which, $r_s=\left(R^2+y_s^2\right)^{1/2}$ and $\theta_s=\tan^{-1}\left(y_s/R\right)$. By making use of Eq. (A6), it is clear that u_x^+ is zero along the wall.

To further demonstrate that the no-flow condition is satisfied, the dimensionless wave elevation in the vicinity of the two symmetrical cylinders is shown in Fig. A1 with $|G_0|$ = 0, e/a = 1, $\kappa_0 a$ = 0.74. In Fig. A1, the incident wave heading varies from β = 0 and π/4. The wave elevation distribution shown in Fig. A1 is symmetric with respect to the y-axis, leading to that along the wall (x = 0) the velocity component in the x-direction is zero.

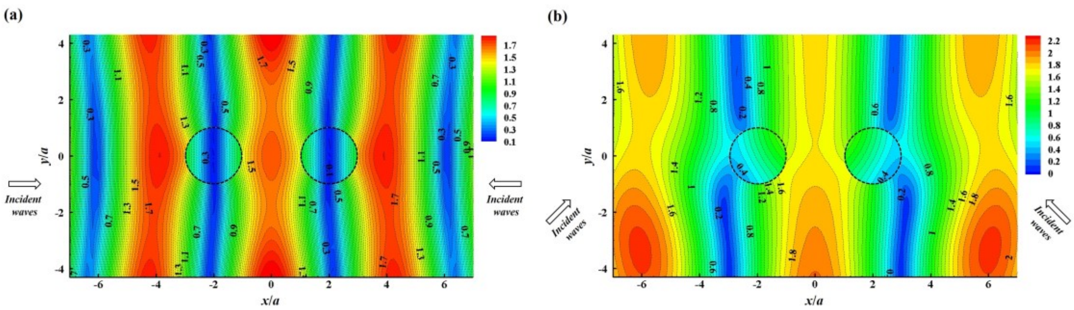

Fig. A1 Magnitude of the dimensionless wave elevation in the vicinity of two symmetrical cylinders with $|G_0| = 0$, $e/a = 1$, $\kappa_0 a = 0.74$ and $d/a = 5$ (a) $\beta = 0$ (b) $\beta = \pi/4$

The wave radiation problem due to the motions of two symmetrical cylinders is then considered. This problem has been discussed in Section 5. In the wave radiation problem, the expression of the velocity potential in Ω^+ has been given in Eq. (30a). Then, for a fluid particel in Ω^+, its velocity component in the x-direction is given by

$$\begin{aligned} \hat{u}_x^+ = & \sum_{j=1}^{N=2} \sum_{m=-\infty}^{+\infty} \hat{A}_{m,\,0}^{j} \left[\kappa_0 H_m' \left(\kappa_0 r_j \right) \cos\theta_j - imH_m \left(\kappa_0 r_j \right) \frac{\sin\theta_j}{r_j} \right] Z_0 \left(\kappa_0 z_j \right) e^{im\theta_j} \\ & + \sum_{j=1}^{N=2} \sum_{m=-\infty}^{+\infty} \sum_{l=1}^{\infty} \hat{A}_{m,\,l}^{j} \left[\kappa_l K_m' \left(\kappa_l r_j \right) \cos\theta_j - imK_m \left(\kappa_l r_j \right) \frac{\sin\theta_j}{r_j} \right] Z_l \left(\kappa_l z_j \right) e^{im\theta_j}. \end{aligned} \tag{A8}$$

In Eq. (A8), the coefficients $A_{m,\,0}^{j}$ and $A_{m,\,l}^{j}$ ($l \geq 1$) can be determined by solving Eqs. (35a) and (36a), respectively. When the two cylinders undergo out-of-phase surge motion, with the information of layout of the cylinders and their radii, Eqs. (35a) and (36a) can be rewritten as

$$\hat{A}_{m,\,0}^{j} p_m + \sum_{n=-M}^{+M} \hat{A}_{n,\,0}^{k} q_{m,\,n}^{j,\,k} = \hat{o}_{m,\,0}^{j,\,k}, \quad j,\ k = 1,\ 2 \text{ and } j \neq k; \tag{A9a}$$

$$\hat{A}_{m,\,l}^{j} \hat{p}_{m,\,l} + \sum_{n=-M}^{+M} \hat{A}_{n}^{k} \hat{q}_{m,\,n,\,l}^{j,\,k} = \hat{o}_{m,\,l}^{j,\,k}, \quad j,\ k = 1,\ 2 \text{ and } j \neq k. \tag{A9b}$$

In Eq. (A9a), the coefficient $\hat{o}_{m,\,0}^{j,\,k}$ is expressed as

$$\hat{o}_{m,\,0}^{j,\,k} = \hat{o}_{-m,\,0}^{k,\,j} = \begin{cases} \dfrac{k-j}{H_m'\left(\kappa_0 a\right)} \Gamma_0, & m = \pm 1, \\ 0, & m \neq \pm 1. \end{cases} \tag{A10}$$

With the application of Eqs. (A4a), (A4b) and A(10) and replacing k, j, m and n in Eq. (A9a) by j, k, $-m$ and $-n$, it can be obtained that

$$\hat{A}_{-m,\,0}^{k} p_m + \sum_{n=-M}^{+M} \hat{A}_{-n,\,0}^{j} q_{m,\,n}^{j,\,k} = \hat{o}_{m,\,0}^{j,\,k}, \quad j,\ k = 1,\ 2 \text{ and } j \neq k; \tag{A11}$$

Eqs. (A9b) and (A11) suggest that the following relationship is held for $\hat{A}_{m,\,0}^{j}$

$$\hat{A}_{m,\,0}^{j} = \hat{A}_{-m,\,0}^{k}, \quad j,\ k = 1,\ 2 \text{ and } j \neq k. \tag{A12}$$

In Eq. (A9b), the coefficients $\hat{p}_{m,\,l}$, $\hat{q}_{m,\,n,\,l}^{j,\,k}$ and $\hat{o}_{m,\,l}^{j,\,k}$ are expressed as

$$\hat{p}_{m,\,l} = \hat{p}_{-m,\,l} = 1 + \frac{i\kappa_0 G_0}{(\kappa_l)^2 a K'_m(\kappa_l a) I'_m(\kappa_l a)}; \tag{A13a}$$

$$\hat{q}^{\,j,\,k}_{m,\,n,\,l} = (-1)^{n-m} \hat{q}^{\,k,\,j}_{-m,\,-n,\,l} = \frac{I'_m(\kappa_l a)}{K'_m(\kappa_l a)} K_{n-m}(2\kappa_l R) e^{\frac{1}{2}i[n(k-j+1)-m(j-k+1)]\pi}; \tag{A13b}$$

$$\hat{o}^{\,j,\,k}_{m,\,l} = (-1)^m \hat{o}^{\,k,\,j}_{-m,\,l} = \begin{cases} \dfrac{k-j}{K'_m(\kappa_l a)} \Gamma_l, & m = \pm 1, \\ 0, & m \neq \pm 1. \end{cases} \tag{A13c}$$

With the application of Eq. (13) and replacing k, j, m and n in Eq. (A9b) by j, k, $-m$ and $-n$, it can be obtained that

$$(-1)^m \hat{A}^k_{-m,\,l} \hat{p}_{m,\,l} + \sum_{n=-M}^{+M} (-1)^n \hat{A}^j_{-n,\,l} \hat{q}^{\,j,\,k}_{m,\,n,\,l} = \hat{o}^{\,j,\,k}_{m,\,l}, \quad j,\ k = 1,\ 2 \text{ and } j \neq k; \tag{A14}$$

Eqs. (A9b) and (A14) suggest that the following relationship is held for $\hat{A}^j_{m,\,l}$

$$\hat{A}^j_{m,\,l} = (-1)^m \hat{A}^k_{-m,\,l}, \quad j,\ k = 1,\ 2 \text{ and } j \neq k. \tag{A15}$$

A location along the wall, with the coordinate (0, y_s, z_s) in the global coordinate system, is concerned again. $\hat{u}^+_x$ at this location can be expressed as

$$\begin{aligned} \hat{u}^+_x &= \sum_{m=-\infty}^{+\infty} \left(\hat{A}^1_{m,\,0} - \hat{A}^2_{-m,\,0}\right) \left[\kappa_0 H'_m(\kappa_0 r_s)\cos\theta_s - imH_m(\kappa_0 r_s)\frac{\sin\theta_s}{r_s}\right] Z_0(\kappa_0 z_s) e^{im\theta_s} \\ &+ \sum_{m=-\infty}^{+\infty} \sum_{l=1}^{\infty} \left[\hat{A}^1_{m,\,l} - (-1)^m \hat{A}^2_{-m,\,l}\right] \left[\kappa_l K'_m(\kappa_l r_s)\cos\theta_s - imK_m(\kappa_l r_s)\frac{\sin\theta_s}{r_s}\right] Z_l(\kappa_l z_s) e^{im\theta_s}, \end{aligned} \tag{A16}$$

After making use of Eqs. (A12) and (A15), it is clear that $\hat{u}^+_x$ is zero along the wall.

When the two cylinders undergo in-phase sway motion, the no-flow condition at the wall can still be satisfied and it can be proved in a similar way to that when undergoing out-of-phase surge motion

Acknowledgement

The work is financial supported by the National Natural Science Foundation of China (Grant Nos. 51809037, 51479026 and 51490672) and Fundamental Research Funds for the Central Universities (DUT18RC(4)048).

Reference

[1] Abramowitz M, Stegun I A. Handbook of Mathematical Functions. Dover Publications, New York, 1972.

[2] An S, Faltinsen O M. An experimental and numerical study of heave added mass and damping of horizontally submerged and perforated rectangular plates. Journal of Fluids and Structures, 2013, 39: 87-101.

[3] Chwang A T. A porous-wavemaker theory. Journal of Fluid Mechanics, 1983, 132: 395-406.

[4] Chen J T, Lin Y J, Lee Y T, Wu C F. Water wave interaction with surface-piercing porous cylinders using the null-field integral equations. Ocean Engineering, 2011, 38(2): 409-418.

[5] Cho I H, Kim M H. Transmission of oblique incident waves by a submerged horizontal porous plate. Ocean Engineering, 2013, 61(2): 56-65.

[6] Cho I H, Kim M H. Wave absorbing system using inclined perforated plates. Journal of Fluid Mechanics, 2008, 608: 1-20.

[7] Darwiche M K M, Williams A N, Wang K H. Wave interaction with semiporous cylindrical breakwater. Journal of Waterway Port Coastal & Ocean Engineering, 1994, 120(4): 382-403.

[8] Evans D V. Asymptotic reflection of linear water waves by submerged horizontal porous plates. Journal of Engineering Mathematics, 2011, 69(2-3):135-154.

[9] Jarlan G E. A perforated vertical wall breakwater. The dock and harbour Authority XII (486), 1961, 394–398.

[10] Kee S T. Submerged plate breakwater composed of horizontal porous plate and slightly inclined solid plate. International Journal of Offshore & Polar Engineering, 2009, 19(1): 42-45.

[11] Koley S, Behera H, Sahoo T. Oblique wave trapping by porous structures near a wall. Journal of Engineering Mechanics, 2015, 141(3): 04014122.

[12] Li Y C, Liu Y, Teng B. Porous effect parameter of thin permeable plates. Coastal Engineering Journal, 2006, 48 (4): 309–336.

[13] Li Y C, Liu H J, Teng B, Sun D P. Reflection of oblique incident waves by breakwaters with partially perforated wall. China Ocean Engineering, 2002, 16 (3): 329–342.

[14] Linton C M., Evans D V. The interaction of waves with arrays of vertical circular cylinders. Journal of Fluid Mechanics 1990, 215: 549–569.

[15] Liu J B, Guo A X, Nandasena N A K, Melville B W, Li H. Theoretical and experimental

investigation on wave interaction with a concentric porous cylinder form of breakwater. Ocean Engineering, 2018, 160: 156-167.

[16] Liu Y, Li H J, Li Y C, He S Y. A new approximate analytic solution for water wave scattering by a submerged horizontal porous disk. Applied Ocean Research, 2011, 33(4): 286-296.

[17] Liu Y, Li Y C, Teng B. The reflection of oblique waves by an infinite number of partially perforated caissons. Ocean Engineering, 2007, 34: 1965-1976.

[18] Liu Y, Li Y C, Teng B. Wave interaction with a perforated wall breakwater with a submerged horizontal porous plate. Ocean Engineering, 2007, 34(17): 2364-2373.

[19] Mandal S, Datta N, Sahoo T. Hydroelastic analysis of surface wave interaction with concentric porous and flexible cylinder systems. Journal of Fluids & Structures, 2013, 42(4): 437-455.

[20] Mei C C, Stiassnie M, Yue D K -P. Theory and applications of ocean surface waves. 2005, World Scientific, Singapore.

[21] Molin B. Hydrodynamic modeling of perforated structures. Applied ocean research, 2011, 33(1): 1-11.

[22] Molin B, Legras J L. Hydrodynamic modeling of the Roseau tower stabilizer. In Proceedings of the 9th international conference on offshore mechanics and arctic engineering (OMAE 1990). 1990, Houston, USA, 329-336.

[23] Molin B, Remy F. Experimental and numerical study of the sloshing motion in a rectangular tank with a perforated screen. Journal of Fluids and Structures, 2013, 43(43): 463–480.

[24] Molin B, Remy F, Rippol T. Experimental study of the heave added mass and damping of solid and perforated disks close to the free surface. In Proceedings of the 12th International Congress of the International Maritime Association of the Mediterranean (IMAM 2007), 2007, Varna, Bulgaria, 879-887.

[25] Neves M D G, Losada I J, Losada M A. Short-wave and wave Group scattering by submerged porous plate. Journal of Engineering Mechanics, 2000, 126(10): 1048-1056.

[26] Ning D Z, Zhao X L, Teng B, Johanning L. Wave diffraction from a truncated cylinder with an upper porous sidewall and an inner column. Ocean Engineering, 2017, 130: 471-481.

[27] Sankarbabu K, Sannasiraj S A, Sundar V. Hydrodynamic performance of a dual cylindrical caisson breakwater. Coastal Engineering, 2008, 55(6): 431-446.

[28] Sankarbabu K, Sannasiraj S A, Sundar V. Interaction of regular waves with a group of dual

porous circular cylinders. Applied Ocean Research, 2007, 29(4): 180-190.

[29] Song H, Tao L B. Short-crested wave interaction with a concentric porous cylindrical structure. Applied Ocean Research, 2007, 29(4): 199-209.

[30] Teng B, Ning D Z. Wave diffraction from a uniform cylinder in front of a vertical wall. The Ocean Engineering, 2003, 21(4): 48-52.

[31] Teng B, Ning D Z, Zhang X T. Wave radiation by a uniform cylinder in front of a vertical wall. Ocean Engineering, 2004, 31: 201-224.

[32] Teng B, Zhang X T, Ning D Z. Interaction of oblique waves with infinite number of perforated caissons. Ocean Engineering, 2004, 31(5): 615-632.

[33] Vijayalakshmi K, Neelamani S, Sundaravadivelu R, Muarli K. Wave runup on a concentric twin perforated circular cylinder. Ocean Engineering, 2007, 34(2): 327-336.

[34] Wang K H, Ren X. Wave interaction with a concentric porous cylinder system. Ocean Engineering, 1994, 21(4): 343-360.

[35] Williams A N, Li W. Wave interaction with a semi-porous cylindrical breakwater mounted on a storage tank. Ocean Engineering, 1998, 25(2–3): 195-219.

[36] Williams A N, Li W. Water wave interaction with an array of bottom-mounted surface-piercing porous cylinders. Ocean Engineering, 2000, 27(8): 841-866.

[37] Yip T L, Chwang A T. Perforated Wall Breakwater with Internal Horizontal Plate. Journal of Engineering Mechanics, 2000, 126(5): 533-538.

[38] Yu X P. Diffraction of water waves by porous breakwaters. Journal of Waterway Port Coastal and Ocean Engineering, 1995, 121(6): 275-282.

[39] Yu X P, Chwang A T. Water waves above submerged porous plate. Journal of Engineering Mechanics, 1994, 120(6): 1270-1282.

[40] Zhao F F, Kinoshita T, Bao W G, Wan R, Liang Z L, Huang L Y. Hydrodynamics identities and wave-drift force of a porous body. Applied Ocean Research, 2011, 33(3): 169-177.

[41] Zhao F F, Zhang T Z, Wan R, Huang L Y, Wang X X, Bao W G. Hydrodynamic loads acting on a circular porous plate horizontally submerged in waves. Ocean Engineering, 2017, 136: 168-177.

[42] Zhao F F, Bao W G, Kinoshita T, Itakura H. Interaction of waves and a porous cylinder with an inner horizontal porous plate. Applied Ocean Research, 2010, 32(2): 252-259.

[43] Zhao F F, Kinoshita T, Bao W G, Huang L Y, Liang Z L, Wan R. Interaction between waves and an array of floating porous circular cylinders, China Ocean Engineering, 2012, 26(3): 397-412.

[44] Zheng S M, Zhang Y L. Wave diffraction from a truncated cylinder in front of a vertical wall. Ocean Engineering, 2015, 104: 329-343.

[45] Zhong Z, Wang K H. Solitary wave interaction with a concentric porous cylinder system. Ocean Engineering, 2006, 33(7): 927-949.